



The completed SDSS-IV extended Baryon Oscillation Spectroscopic Survey: a catalogue of strong galaxy–galaxy lens candidates

Michael S. Talbot,¹ Joel R. Brownstein¹ , ¹★ Kyle S. Dawson,¹ Jean-Paul Kneib² and Julian Bautista

¹Department of Physics and Astronomy, University of Utah, 115 S. 1400 E., Salt Lake City, UT 84112, USA

²Institute of Physics, Laboratory of Astrophysics, Ecole Polytechnique Fédérale de Lausanne (EPFL), Observatoire de Sauverny, CH-1290 Versoix, Switzerland

³Institute of Cosmology & Gravitation, University of Portsmouth, Dennis Sciama Building, Portsmouth PO1 3FX, UK

Accepted 2021 January 26. Received 2021 January 26; in original form 2020 July 28

ABSTRACT

We spectroscopically detected 838 likely, 448 probable, and 265 possible strong lens candidates within ≈ 2 million galaxy spectra contained within the extended Baryon Oscillation Spectroscopic Survey (eBOSS) from the sixteenth data release (DR16) of the Sloan Digital Sky Survey (SDSS). We apply the spectroscopic detection method of the Baryon Oscillation Spectroscopic Survey (BOSS) Emission-Line Lens Survey (BELLs) and add Gaussian fit information, grading, additional inspection observables, and additional inspection methods to improve our selection method. We observed 477 candidates with lensing evidence within low-resolution images from both the Legacy survey of SDSS-I/II and the DESI Legacy survey, which is 12 per cent higher than the percentage of BELLs candidates observed with similar lensing evidence. Our search within the latest and improved reductions of the BOSS survey yielded a 20 per cent increase in the number of lens candidates expected from searching all BOSS and eBOSS galaxies. The distribution of target and background redshifts of our candidates is similar to the candidates and confirmed lenses within the BELLs observations. We present our Spectroscopic Identification of Lensing Object candidates in a value-added catalogue in SDSS DR16. The examination of these lens candidates in follow-up high-resolution imaging may yield more than twice the lenses found in previous spectroscopic detection surveys within SDSS, which would extend the results of previous lens surveys within SDSS to higher redshifts, constrain models of mass structures in spiral galaxies, and test if including the identification of possible lensing features within low-resolution images has merit to spectroscopic detection programmes.

Key words: gravitational lensing: strong – galaxies: general – cosmology: miscellaneous.

1 INTRODUCTION

1.1 The spectroscopic identification of lensing objects

We are interested in the many ways that galaxy-scale strong gravitational lensing enables the measurement of the galactic mass distribution, and to decompose the dark matter distribution to explore the effect on galaxy formation and evolution, and to use this data to refine the standard model of cosmology to further our understanding of the distribution of matter in the Universe. We are also interested in how precise gravitational lensing models may test general relativity and gravity theories.

Obtaining large samples of confirmed galaxy-scale lenses with Einstein radii distributed across the radial extent of the galactic profiles would enable us to probe further into the baryon-dominated galaxy core and also out farther into the dark matter dominated halo. An effective way to acquire this needed spread, commonly parametrized by the ratio of Einstein radii to the effective radius, is to search large surveys for galaxy–galaxy strong lenses across several ranges of redshift, which also enables us to measure distance and time-dependent trends in the galaxy structure, to study galaxy formation and evolution, and cosmology-scale properties.

Our overall project objective is to discover and confirm $\mathcal{O}(10^3)$ grade-A strong gravitational lenses within the Sloan Digital Sky Survey (SDSS) including the SDSS-I/II Legacy (Lupton et al. 2001) survey, the Baryon Oscillation Spectroscopic Survey (BOSS; Dawson et al. 2013) from SDSS-III, the extended Baryon Oscillation Spectroscopic Survey (eBOSS; Dawson et al. 2016), and the Mapping Nearby Galaxies at APO (MaNGA; Bundy et al. 2015) survey of the current phase of the Sloan Digital Sky Survey (SDSS-IV; Blanton et al. 2017). Such a catalogue would be the first of its kind, and the current version is available to the public, included in the Sixteenth Data Release (DR16) of the SDSS-IV (Ahumada et al. 2020). We provide a brief overview of galaxy–galaxy strong gravitational lensing in Section 1.2 and review the progress of the spectroscopic detection method in SDSS in Section 1.3.

1.2 Galaxy–galaxy strong gravitational lensing

The gravitational bending of the light from a distant source galaxy as it passes near the influential mass of the lens galaxy can generate multiple images of the source at the position of an observer along the line-of-sight (LOS) of the converging rays from the images. These strong galaxy-scale gravitational lenses will magnify at least one of the warped source images. In addition, grade-A lenses clearly demonstrate multiple source images that can be modeled to provide

* E-mail: joelbrownstein@astro.utah.edu

precise values of the Einstein radii, which are used as mass probes into individual galaxies and cosmological parameters, including the expansion rate of the Universe that influences the difference in the arrival time of light between multiple source images. These properties of galaxy–galaxy strong gravitational lenses have been used to constrain cosmology and galaxy evolution in a variety of ways, such as:

(i) Using the lens as a telescope to examine magnified spacial or spectral features of galaxies (which may be unresolved without lensing) to study source properties such as star formation, stellar populations, size and compactness of the source, and classify source into categories such as a compact blue dwarf, a low-metallicity star-bursting dwarf galaxy, or an early-type galaxy (Marshall et al. 2007; Cabanac, Valls-Gabaud & Lidman 2008; Brammer et al. 2012; Oldham et al. 2017; Cornachione et al. 2018).

(ii) Fitting a galaxy mass model to how the lens is bending the source light to measure the total mass scale and mass distribution of the lens, determined by the best-fitting model. These measurements can then be combined with the lens’ light profile to determine the total mass-to-light ratio. Fitting stellar (and even gas) mass models to the light from the lens enable the lens mass to be separated into the contributions from baryons and dark matter. All of these measured components can be used to test and constrain models of the mass structure of galaxies, which impact galaxy formation and evolution models (Kochanek 1995; Gavazzi et al. 2008; Lagattuta et al. 2012; Nightingale et al. 2019).

(iii) Combining lensing with rotation curves or other dynamic and kinematic data to significantly constrain measurement uncertainties and enable the dissection of the mass distribution into the different stellar, gaseous, morphological, and dark components of galaxies (Dutton et al. 2011; Spinelli et al. 2011; Barnabè et al. 2012).

(iv) Measuring the mass distributions of a large set of lenses (which can be combined with dynamical mass measurements) across cosmological redshifts enables a probe into trends within galactic mass profiles across distance and time. This information is useful to constrain time and distance independent or dependent mass components of galaxy structure, formation, and evolution models (Keeton & Kochanek 1998; Keeton, Kochanek & Falco 1998; Koopmans et al. 2006; Bolton et al. 2008b; Barnabè et al. 2009; Koopmans et al. 2009; Auger et al. 2010; Sonnenfeld et al. 2013; Shu et al. 2015; Cao et al. 2016; Li, Shu & Wang 2018; Mukherjee et al. 2019; Sonnenfeld et al. 2019).

(v) Probing possible indications of dark matter haloes perturbing the source light along the line-of-sight (LOS; Despali et al. 2018).

(vi) Probing for dark substructures near or within the lens using methods such as gravitational imaging (Koopmans 2005; Vegetti et al. 2010, 2014; Hezaveh et al. 2016).

(vii) Detecting dark satellite galaxies perturbing the path of the source light (Vegetti et al. 2012).

(viii) Using the time-difference measured between flux-varying source images to better constrain angular diameter distances and components in the lens model (Jee, Komatsu & Suyu 2015).

(ix) Testing the cosmological constant Λ in the standard model of cosmology by comparing lens statistics to derived expectations (Fukugita, Futamase & Kasai 1990).

(x) Providing insights that help refine concepts related to Cold Dark Matter (Λ CDM) models (Benson 2020).

(xi) Constraining the dark energy equation of state and other components of cosmography by examining rare lenses with two sources (Gavazzi et al. 2008; Collett et al. 2012; Linder 2016).

Most of the research efforts listed above utilize large samples of lenses to either observe trends in galactic mass profiles or to search for unusual lens systems within the sample. Obtaining large samples of galaxy-scale strong gravitational lenses is difficult, since a source galaxy has to be sufficiently distant from the lens galaxy with an alignment within arc-seconds of the line of sight from the lens galaxy to the distant observer. Most of these chance alignments are unlikely to be detected within images, since the dominating foreground light of the lens galaxy often conceals most or all of the background source light. It is also difficult to differentiate unclear features of a source from either an un-lensed background galaxy, multiple background galaxies, satellite galaxies, structure in the lens, improper image reduction, or other causes of false-positive features.

1.3 Spectroscopic detection within SDSS

One of the most successfully tested solutions to obtain a large sample of confirmed galaxy-scale lenses is to spectroscopically detect background emission lines from star-forming galaxies behind the target galaxy within a sample on the order of a million galaxy spectra, followed by precisely subtracting the foreground lens light in follow-up high-resolution images to confirm the source.

The Sloan Digital Sky Survey (SDSS; York et al. 2000) contains the largest fraction of confirmed lenses, with at least 145 grade-A strong galaxy-scale lenses confirmed from at least 311 lens candidates spectroscopically detected by the Sloan Lens ACS (SLACS; Bolton et al. 2006) survey, the Sloan WFC Edge-on Late-type Lens Survey (SWELLS; Treu et al. 2011), and the SLACS for the Masses (S4TM; Shu et al. 2015) survey within the ≈ 1 million galaxy spectra ($z < 0.55$) contained in the Legacy survey of SDSS-I/II. These lens surveys verified the source images after subtracting the lens light in follow-up images obtained either by the Hubble space telescope (*HST*) or Keck-II.

Moving out to greater target redshifts in the SDSS-III/IV era, the BOSS and eBOSS surveys used the BOSS spectrograph (Gunn et al. 2006; Smee et al. 2013) to provide more than twice as many galaxy spectra up to twice the redshift ($z < = 1.1$) of the galaxy sample contained within the Legacy survey of SDSS-I/II. The BOSS Emission-Line Lens Survey (BELLS; Brownstein et al. 2012), based on the spectroscopic detection method of the SLACS survey, yielded 25 grade-A strong galaxy–galaxy scale gravitational lenses from 45 lens candidates at the start of the BOSS survey following the Ninth Data Release (DR9), which contained only $\frac{1}{17}$ of the galaxy spectra of the now completed BOSS and eBOSS surveys in DR16. The BELLS lenses were confirmed by *HST* Program 12209, including precise lens models constructed after subtracting the foreground lens light in the follow-up images.

Several other lensing surveys have successfully identified a fraction of the spectroscopically detectable candidates within the BOSS survey. The BELLS GALaxy-Ly α EmittErs YStems (BELLS GALLERY; Shu et al. 2016) survey found 21 strong gravitational lens candidates (17 confirmed) with candidate Ly α emitters (LAEs) sources by searching for Ly α emissions behind the target. The Survey of Gravitationally lensed Objects in HSC Imaging (SuGOHI; Sonnenfeld et al. 2018) survey has developed a combined image and spectrum search method that included a spectroscopic search of $\frac{1}{20}$ of the BOSS targets. Thus, the remaining $\frac{15}{17}$ of the BOSS and eBOSS targets were not scanned for the emission lines searched within spectroscopic detection surveys prior to the SuGOHI survey (see Table 1).

Table 1. Emission lines searched for within the BOSS and eBOSS surveys. Column 1 lists the name of each emission line, while Column 2 lists the rest-frame vacuum wavelength of each emission line. Column 3 lists the maximum redshift each emission line can be detected within the BOSS spectrograph.

Emission line	Rest frame wavelength (Å)	z_{\max}
(1)	(2)	(3)
[O II]b	3727.09	1.78
[O II]a	3729.88	1.78
H δ	4102.89	1.52
H γ	4341.68	1.38
H β	4862.68	1.13
[O III]b	4960.30	1.09
[O III]a	5008.24	1.07
[N II]b	6549.86	0.58
H α	6564.61	0.58
[N II]a	6585.27	0.57
[S II]b	6718.29	0.54
[S II]a	6732.68	0.54

This work extends the Spectroscopic Identification of Lensing Objects (SILO; Talbot et al. 2018) programme to complete the search for galaxy–galaxy lens candidates within the latest reductions of the galaxy spectra contained within SDSS-IV Data Release 16 of the completed BOSS and eBOSS surveys. SILO is the current evolution of the SDSS spectroscopic detection code that displays significantly more information on the quality of the candidate emission lines and possible sources of contamination (see Sections 3.3 and 3.5) by means of a manual inspection (PYTHON) interface.

We also inspected low-resolution images of the target to assess if interference from foreground objects may impact the signal and if lensing evidence is observed within the images (see Section 3.6). We created a grading scheme which is calibrated to assign a grade of A- or above to candidates with emission lines as clearly defined as the confirmed emission lines observed within the BELLS survey. We also assign each candidate a total grade based upon the assurances observed within both the signal quality and evidence of lensing.

This paper is organized as follows. The expected number of lenses and lens candidates that SILO can detect within the BOSS and eBOSS surveys are described in Section 2. The spectroscopic detection method is presented in Section 3, consisting of foreground spectrum modelling and subtraction (Section 3.1), background emission-line detection (Section 3.2), Gaussian modelling of the candidate emission lines of the candidate background galaxy (Section 3.3), candidate cuts with respect to likely lensed systems (Section 3.4), inspection method of the spectra (Section 3.5), and inspection of low-resolution images (Section 3.6). We present a summary of our findings in Section 4, consisting of the counts of detected candidates and examples of lens candidates (Section 4.1), counts of the types of features observed in low-resolution images that may be related to lensing (Section 4.2), and comparison of SILO lens candidates to the BELLS survey (Section 4.3). We describe the publicly available value-added catalogue (VAC) containing the BOSS and eBOSS lens candidates in Section 5. We provide a summary and discuss some examples of how follow-up imaging of these lens candidates can extend the results of previous lens surveys, enable new lensing research, and provide opportunities to bridge information from spectroscopic detection with low-resolution images in future discovery programmes (Section 6).

2 EXPECTED NUMBER OF HIGHLY ASSURING LENS CANDIDATES AND CONFIRMABLE GRADE-A LENSES

Since the SILO and BELLS discovery programmes follow a common detection method (see Section 3) to find lenses within SDSS-III BOSS data, we can approximate the number of BOSS lens candidates SILO should detect by scaling up the number of lens candidates found in the BELLS survey by the fractional increase of SDSS-III BOSS galaxies searched by SILO over the BELLS survey, which was limited to DR10. The ≈ 1.5 million galaxy spectra of the improved [see reduction improvements in Ahn et al. (2014), Alam et al. (2015), Albareti et al. (2017), Abolfathi et al. (2018)] and final DR16 data reduction pipeline ($v5_13.0$) contains 13 times the luminous-red-galaxy (LRG) spectra available to the BELLS. If we neglect the additional inspection methods, additional spectral observables, additional image observables, and improved pipeline of the BOSS data, then we expect SILO to result in spectroscopically selecting $\approx 13 \times 45 = 585$ lens candidates within the BOSS data, with a similar quality of signal to the BELLS candidates. Since 25 (56 per cent) of the lens candidates from the BELLS survey were confirmed as grade-A lenses, we can extrapolate that approximately $\approx 13 \times 25 = 325$ of SILO lens candidates would be confirmed as grade-A lenses under the same assumptions as above. We do not remove any previously discovered candidates from this approximation, since previously discovered candidates are included in the DR16 results, in order to provide a self-consistent and complete VAC to the public, as a comparative resource.

In addition to the SDSS-III BOSS data, DR16 contains 0.5 million galaxy spectra targeted by the SDSS-IV extended BOSS (eBOSS) survey, which is $\frac{1}{4}$ the number of galaxy spectra contained within the BOSS survey. Thus the total galaxy spectra contained in DR16, which includes all of the BOSS and eBOSS targets, and searched by SILO, is a factor of seventeen more than the galaxy spectra searched by the BELLS. However, several differences between the BOSS and eBOSS galaxies imply that the SILO detection rate for eBOSS targets will be significantly reduced by the following limiting factors:

(i) The target selection of eBOSS galaxies is extended to higher redshifts by +0.4. The higher redshifts of the eBOSS targets require the redshift of any background source to typically be higher than in BOSS targets for strong lensing to occur. Thus, the search window between the lower redshift limit of candidate eBOSS sources and the maximum limit of the spectrograph is typically smaller for eBOSS targets than for BOSS targets.

(ii) Sixty per cent of the eBOSS targets are emission line galaxies (ELG), which are typically less massive than the luminous red galaxies (LRG) from the BOSS survey. Thus, the fraction of background sources whose signal was magnified by lensing above our detection threshold will be less for eBOSS galaxies in comparison to BOSS galaxies since the lower ELG masses will decrease the magnification power of the lens, and reduce the Einstein radius of lenses within the eBOSS survey.

It is important to note that a typically smaller Einstein radius for eBOSS candidates may enable more sources to be found within the 1 arcsec solid angle of the spectroscopic fibre. However, blurring from seeing mitigates this advantage since sources beyond the solid angle of the fibre can be ineffectively detected (Arneson, Brownstein & Bolton 2012). Thus, the significant differences listed above imply that SILO should find less than $585 \times \frac{1}{4} = 146$ lens candidates from eBOSS galaxies with quality of signal similar to that of the BOSS candidates, though it is reasonable to speculate that

we will select on the order of a hundred eBOSS candidates. Thus, the sum of our approximations yields a total expectation of ≈ 700 SILO lens candidates with quality of signal approximate to the BELLS candidates of which $\approx 325 + \approx 50 = \approx 375$ can be expected to be confirmed as grade-A lenses.

We emphasize that the actual yield of candidates from SILO should be greater than the above estimate, since we used the improved final (*v5_13_0*) data reductions of the BOSS and eBOSS spectra released with DR16, and included additional observables in the spectroscopic lens detection method. We also emphasize these estimations apply only to candidates with quality of signal approximate to the BELLS candidates, and thus the expected number of lens candidates may be better treated as a lower bound to the number of lens candidates and grade-A lenses that can be found by SILO. Results from the SLACS survey demonstrate that the spectroscopic detection rate is approximately 1 in 1000 galaxy targets within the Legacy survey of SDSS-I/II (Bolton et al. 2006; Marshall et al. 2009). Since the spectroscopic detection window between the Legacy and BOSS surveys remained approximately the same, we can speculate that the number of spectroscopically detectable lenses within BOSS and eBOSS is within an order of magnitude of 2000 strong gravitational lenses.

3 SPECTROSCOPIC CANDIDATE SELECTION

The approach of our spectroscopic detection method is to search for background emission lines within the solid angle of the fibre (see also Warren et al. 1996; Hewett et al. 2000; Willis, Hewett & Warren 2005; Willis et al. 2006). We first summarize our spectroscopic discovery method and then proceed to describe each step. We searched for strong galaxy–galaxy gravitational lenses within the co-added galaxy spectra contained within the completed BOSS and eBOSS surveys within the SDSS DR16 data set. Our selection method is based upon the spectroscopic detection method, refinement cuts, and manual inspection method of the BELLS programme, which were extended from the methods of the SLACS survey. The spectroscopic detection method fits a multicomponent galaxy template model to the foreground flux, then removes the flux according to the model, and then searches the residual flux for higher redshift, high signal-to-noise (SN) gas emission lines of a star-forming galaxy that is sufficiently distant behind the foreground galaxy for strong lensing to likely occur. Since the fibre radius, exposure times, and the BOSS spectrograph are unchanged between the SDSS-III and the current search of SDSS-IV, our application of the BELLS discovery method recovered a similar SN for the emission lines of the candidates from the BELLS detections.

We add best-fitting Gaussian models to the detected background emission lines, additional observables of the spectra, low-resolution images of the target, and additional inspection methods to the BELLS inspection process. Detections that are likely sky, target emission lines, misidentified background emission lines, are unlikely to originate from background galaxies, or are unlikely to be strongly lensed are rejected in the refinement cuts, manual inspection of the spectra, and image inspection processes. The solid angle of the 1 arcsec fibre, which is ineffectively extended by seeing (Arneson et al. 2012), limits the LOS of the candidate background galaxy to near or often within the strong lensing regime, which enables us to promote the candidate background galaxies to strong galaxy–galaxy scale gravitational lens candidates as has been done in previous spectroscopic detection surveys within SDSS.

3.1 Foreground galaxy subtraction

We model and subtract the spectra of the foreground galaxy using the SILO code, which includes a PYTHON re-implementation of the IDL algorithms common to SLACS, SWELLS, S4TM, BELLS, and BELLS GALLERY. We first mask the contaminated parts of the co-added spectra using the ANDMASK supplied for each target from the BOSS and eBOSS surveys. We then construct a principal component analysis (PCA) model of the foreground galaxy spectra using the precise spectroscopic redshift obtained by the spec1d (Bolton et al. 2012) data reduction pipeline using a basis of 7 PCA eigenspectra derived from SDSS galaxies. Finally, we use the constructed galaxy model to subtract the light of the foreground galaxy, which produces a flattened residual flux that is dominated by noise.

3.2 Background emission-line detection

The primary objective of our spectroscopic detection method is to find emission lines from a galaxy far behind the target, which are caused when large, hot, and newly formed main sequence stars (i.e. such as O, B, and A stars) heat and photoionize the surrounding gas into emission. Since the background emission lines are not removed in foreground subtraction, these emission lines can appear as high SN features within the residual flux. We compute the SN of the spectra and then search for

- (i) two or more of the emission lines listed in Table 1 with an SN ≥ 4 ;
- (ii) an [O II](b, a) doublet with an SN ≥ 6 .

This yields a precise redshift for the candidate background source galaxy.

The S/N thresholds are identical to the SLACS and BELLS surveys and are selected to maximize the detection of lensed galaxies while preventing false-positives from dominating the catalogue of candidates. The first and second search modes are known as ‘multi-line’ and ‘single-line’ detections, respectively. We require the redshift of these detections to be at least 0.05 behind the target as also required within the BELLS survey. This automatic search of DR16 produced 76 889 single-line detections and 49 732 multi-line detections.

3.3 Fitting Gaussian models to the detections

We added Gaussian fit information to our candidate selection method to highlight more promising or questionable features in the detections and observe global trends in the signal (see Section 3.5). We first fit all candidate background emission lines to a single Gaussian by minimizing the $\tilde{\chi}^2$ of the fit. The inverse-variances used in the $\tilde{\chi}^2$ fit enabled us to automatically reject bad data inherent to the data reduction pipeline. We also fit the [O II](b, a) candidate emission lines to a [O II](b, a) double Gaussian with a fixed 1:1 amplitude ratio and a redshift-dependent separation between the modelled emission lines. These constraints enabled us to use the reduced $\tilde{\chi}^2$ of the fits within three sigma of the model (including the emission-line spacing for the double Gaussian model) to infer whether the following constraints are met:

- (i) The candidate [O II](b, a) doublet approximately matches the [O II](b, a) pattern expected from a star-forming galaxy.
- (ii) The shape of the candidate [O II](b, a) doublet yields smaller errors of the fit to an [O II](b, a) double Gaussian than a single Gaussian.

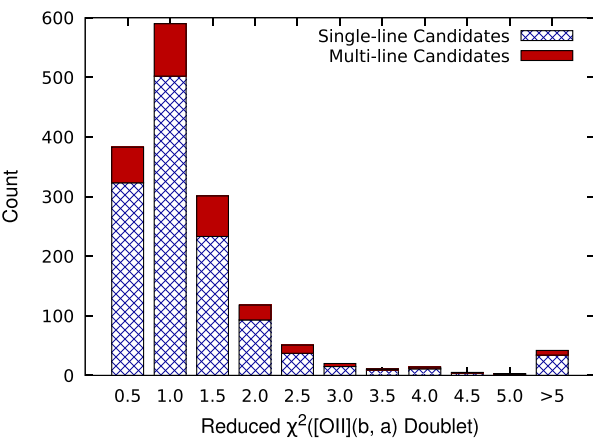


Figure 1. Histogram demonstrating the quality of the [O II](b, a) doublet Gaussian fit to the candidate [O II](b, a) doublets. Candidates are binned by the reduced χ^2 of the fit evaluated within three σ_{model} of the emission lines. The blue patch pattern and solid red pattern represents which portion of each bin count is found by single-line or multi-line search modes, respectively. The reduced χ^2 of the fit is less than three for 94 per cent of the candidate [O II](b, a) doublets.

In contrast, these constraints do not enable the variance in the observed amplitudes of the candidate [O II](b, a) doublet Gaussian to be fitted individually. Thus, while these constraints are ideal for comparing the quality of the fit with the expected pattern of an [O II](b, a) doublet, we emphasize that the observed details in the features of candidate [O II](b, a) doublets can be misrepresented by the fit. It is also important to note that we fit the candidate emission lines as observed, which are not re-scaled into the candidate rest-frame of the emission. An explanation of the optimization method to perform the fit is presented in Appendix A.

The best-fitting Gaussian parameters are included in the VAC (see Section 5) to provide users with an indicator of the quality of the expected patterns demonstrated by the emission line(s) within the SILO candidates. We also provide an approximation of the uncertainty in the parameters by computing the difference between the best-fitting parameters and the 16 and 84 quartiles of each parameter evaluated from 10 000 samples generated by Monte Carlo simulations. The Monte Carlo samples were generated by adding error-scaled Gaussian noise to the residual flux and performing the fit. Fig. 1 demonstrates the quality of the [O II](b, a) doublet Gaussian fit to the [O II](b, a) candidates.

3.4 Refining pre-inspection detections

We filter detections with the same initial, pre-inspection cuts applied in the BELLS method, which reject:

- (i) Single-line detections whose candidate [O II](b, a) doublet is near an unusually high occurrence of detections in the observed-frame, which is more likely explained as an undersubtracted sky emission or un-masked instrument contamination.
- (ii) Single-line detections whose candidate [O II](b, a) doublet is near an unusually high occurrence of detections in the rest frame, which is more likely explained as contamination from target emission lines that are not masked in the detection method.
- (iii) Single-line detections located at the same wavelength as a multi-line detection within the same target.
- (iv) Single-line detections that indicate an [O II](b, a), H δ , [O III]a, or H α emission line with an SN ≥ 3 is present when the candidate

[O II](b, a) doublet is tested as a misidentified H δ , [O III]a, or H α emission line.

- (v) Whose test Einstein radius (computed using a fiducial velocity dispersion of 250 km s $^{-1}$) is less than 450 Kpc.

These cuts reduce the number of single-line and multi-line detections from 76 889 and 49 732 to 3730 and 2841, respectively, which can then be manually inspected as a more manageable number.

3.5 Visual inspection of spectra

We follow the inspection methods of the BELLS survey in our manual inspection process, as stated below:

- (i) ‘Visually inspect the reduced spectra of all remaining selected systems at the position of the candidate background emission lines, to remove obvious data-reduction/data-quality artefacts.’
- (ii) ‘Inspect neighbouring fibre spectra on each plate at the wavelength of the candidate background emission to rule out cross talk from bright emission lines in neighbouring spectra, and spatially localized auroral emission not subtracted by the global sky spectrum model.’
- (iii) ‘Inspect the individual exposure spectra that were co-added to give the final detection spectrum, to ensure that the candidate background emission-line feature is not present in only a single frame (as would be expected for e.g. cosmic ray hits).’
- (iv) ‘Inspect the raw spectroscopic CCD data for all exposures at the position of [O II] $\lambda\lambda$ 3727 emission for single-line candidates, to ensure that the detection is not related to cosmetic blemishes in the CCD.’

We included more observables in the SILO inspection process in an effort to better assess the isolation of real emission lines of the background galaxy, improve the rejection efficiency of false detections, and gain more insight into subtle sources of contamination. The additional methods and observables we examined are listed below, in which we clarify here that references of ‘sky’ in the list below refer to atmosphere emissions. We also provide a quality of assurance that the signal of the detection is from a background galaxy by assigning a grade of assurance (see grading criteria in Table B1) and inspection comment. The grading scheme is intended to assign an A- or higher to detections with clarity of signal approximate to the BELLS candidates. The grade assigned to each detection is dependent on the number of candidate emission lines observed, how clearly the candidate’s signal matches the emission-line patterns of a star-forming galaxy, and how isolated is the signal from regions of potential contamination. The assigned grade represents the combined assurances from the BELLS inspection methods and the additional methods are listed here:

- (i) Simultaneously examine the number, quality, SN (to assess if lensing might be magnifying the signal), patterns demonstrated, and isolation of all candidate emission lines listed in Table 1 that are observed within the spectra whether the S/N of each candidate emission line is weak or strong. This additional step enables the inspector to observe additional candidate emission lines below the detection threshold to better assess the assurances of detections, which is particularly beneficial to assess single-line detections that are relatively more prone to misidentification than multi-line detections.
- (ii) Examine each spectrum with the ANDMASK (obtained from the BOSS and eBOSS surveys) to flag the proximity of known sky/calibration/instrumental artefacts to each candidate emission

Table 2. Count of strong lensing candidates within each grade and line search method. Column 1 lists the grade of assurance that the candidate background galaxy is strongly lensed. Columns 2 and 3 list the count of strong lensing candidates, binned by spectroscopic grade and total grade (combining the spectroscopic with imaging grade), respectively, which contained multiple emission lines with an $SN \geq 4$. Columns 4 and 5 list the count of strong lensing candidates, binned by spectroscopic grade and total grade, respectively, which contained an [O II](b, a) doublet with an $SN \geq 6$.

Grade (1)	Multi-line candidates		Single-line candidates	
	Spectroscopic grade (2)	Total grade (3)	Spectroscopic grade (4)	Total grade (5)
A+	105	125	105	205
A	58	49	277	257
A-	47	43	246	240
B+	16	16	138	134
B	15	13	95	90
B-	15	18	169	158
C+	14	11	101	87
C	8	5	67	53
C-	10	8	65	39
Total	288	288	1263	1263

Table 3. Counts and comparison to the control sample of the lensing evidence observed within low-resolution images of the lens candidates. Column 1 lists the type of lensing evidence observed. Columns 2, 4, and 6 lists the count of clearly visible, discernible, and emergent types of lensing evidence observed in the SILO candidates, respectively. Columns 3, 5, and 7 lists the clearly visible, discernible, and emergent, respectively, ratios of the number density of the type of lensing evidence observed in the lens candidates to the number density of lensing evidence observed in 10 000 randomly selected galaxies from the BOSS and eBOSS surveys. An ‘NA’ implies the specified evidence of lensing was not observed within the 10 000 randomly selected galaxies.

Lensing evidence indicated (1)	Clearly visible		Discernible		Emergent	
	Count (2)	$\frac{\rho_N \text{ in Candidates}}{\rho_N \text{ in Control}}$ (3)	Count (4)	$\frac{\rho_N \text{ in Candidates}}{\rho_N \text{ in Control}}$ (5)	Count (6)	$\frac{\rho_N \text{ in Candidates}}{\rho_N \text{ in Control}}$ (7)
Ring	0	NA	5	10X	7	3X
Multiple images or arcs	3	NA	7	15X	19	26X
Arc	3	18.4X	34	8.4X	63	5X
Possible source radially nearby the lens	8	3X	75	2X	46	1X
Possible overlapping colours of two galaxies	3	2X	26	3X	178	3X
Total	17		147		313	

line. This step highlights potential artefacts that might not be eliminated entirely from the co-added spectrum.

(iii) Examine each spectrum with the ORMASK (obtained from the BOSS and eBOSS surveys) to flag the proximity of known cosmic rays and other issues that might alter the appearance of the signal. This step is redundant with the BELLS selection method but is useful to demonstrate that an issue is apparent.

(iv) Examine enhanced subtle variances in the raw CCD frame at the region of the candidate [O II](b, a) doublet within each exposure. This step revealed subtle events of contamination that are not detected within the reduction pipeline and are hard to observe in the raw frame without stretching the intensity of the image by the local sigma around the local median.

(v) Compare the proximity, alignment, pattern, and relative amplitude of any candidate emission line near or over sky emissions to determine how likely each candidate emission line may be explained as contamination from undersubtraction of sky emissions. We also compare the uncalibrated and calibrated sky spectra to reveal regions of unusual sky calibration. Trends observed in the patterns of sky contamination enable us to better calibrate the inspection process during the re-evaluation of the candidates (see Section 3.7).

(vi) If we suspected a reduction issue, we compared how the signal of the detection translates between the raw CCD frame, the individual exposures, and the co-added spectra to learn how potential

contamination may be introduced during data reduction. Observed trends in the indications of reduction contamination enable us to better calibrate the inspection process during the re-evaluation of the candidates (see Section 3.7).

(vii) Examine the calibration vector to notice any calibration variances at the location of each candidate emission line.

(viii) Examine the wavelength dispersion of the spectra located near the candidate to observe any variances that can impact the measurement of the flux.

(ix) Examine if the signal is near an unusually high occurrence of either detections or detections that passed the first iteration of inspection (see Section 3.7), which cannot be justified by relatively lower noise in the region caused by less intense or fewer sky emissions. This step helps the inspector identify regions of known and unknown contamination that are too insignificant to be filtered in the pre-inspection cuts.

(x) Examine the proximity of all candidate emission lines in Table 1 to 172 emission lines observed in the spectra of galaxies, Active Galactic Nuclei (AGN), and Quasi-Stellar Objects (QSOs) (Ferland & Osterbrock 1987; Osterbrock & Pogge 1985; Rose et al. 2011; Komossa et al. 2008; Alloin et al. 1992; Wang et al. 2011; Izotov et al. 2004; Izotov, Chaffee & Schaefer 2001; Puchnarewicz, Mason & Siemiginowska 1998; Thuan & Izotov 2005; Leighly & Moore 2004; Tran, Cohen & Villar-Martín 2000;

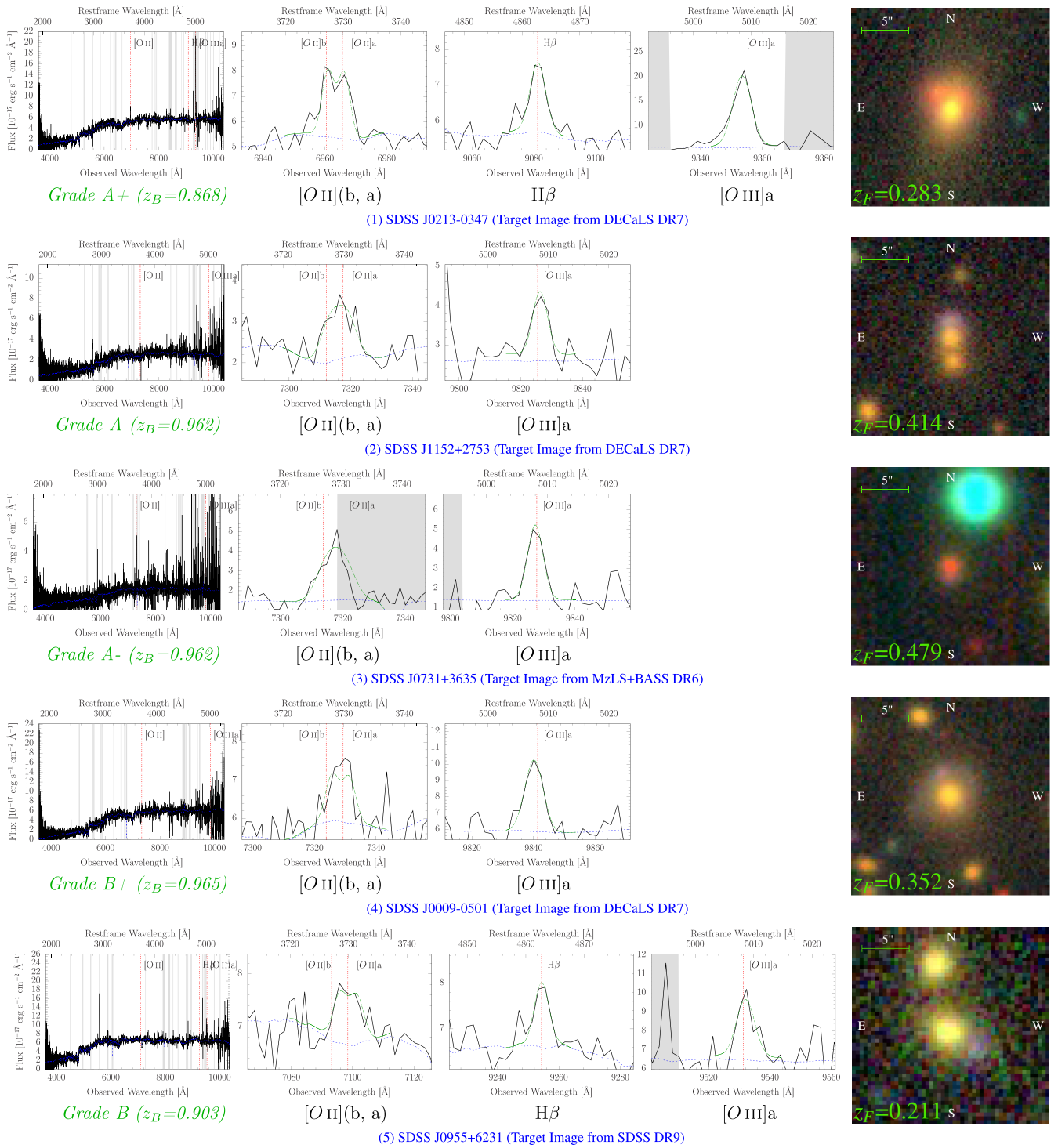


Figure 2. Examples of multi-line lens candidates, sorted by grade and selected in favour of candidates that might demonstrate a potential feature of lensing within a low-resolution image. Left: Plot of the target spectra and the position of the candidate background emission lines with an $SN \geq 4$. The grade and redshift are displayed below the plot in green. Centre: Plot of the flux, target model, and the appropriate Gaussian plus continuum model for each candidate emission line with an $SN \geq 4$. Within these plots, we represent the spectra with a black line, the foreground model with a dashed blue line, the fitted Gaussian model with a green dash-dotted line, and the positions of the candidate background emission lines with an $SN \geq 4$ with a red dotted vertical line. Masked regions of the flux are shaded with grey regions, which were not used in the generation of the background emission-line detections. This figure is continued.

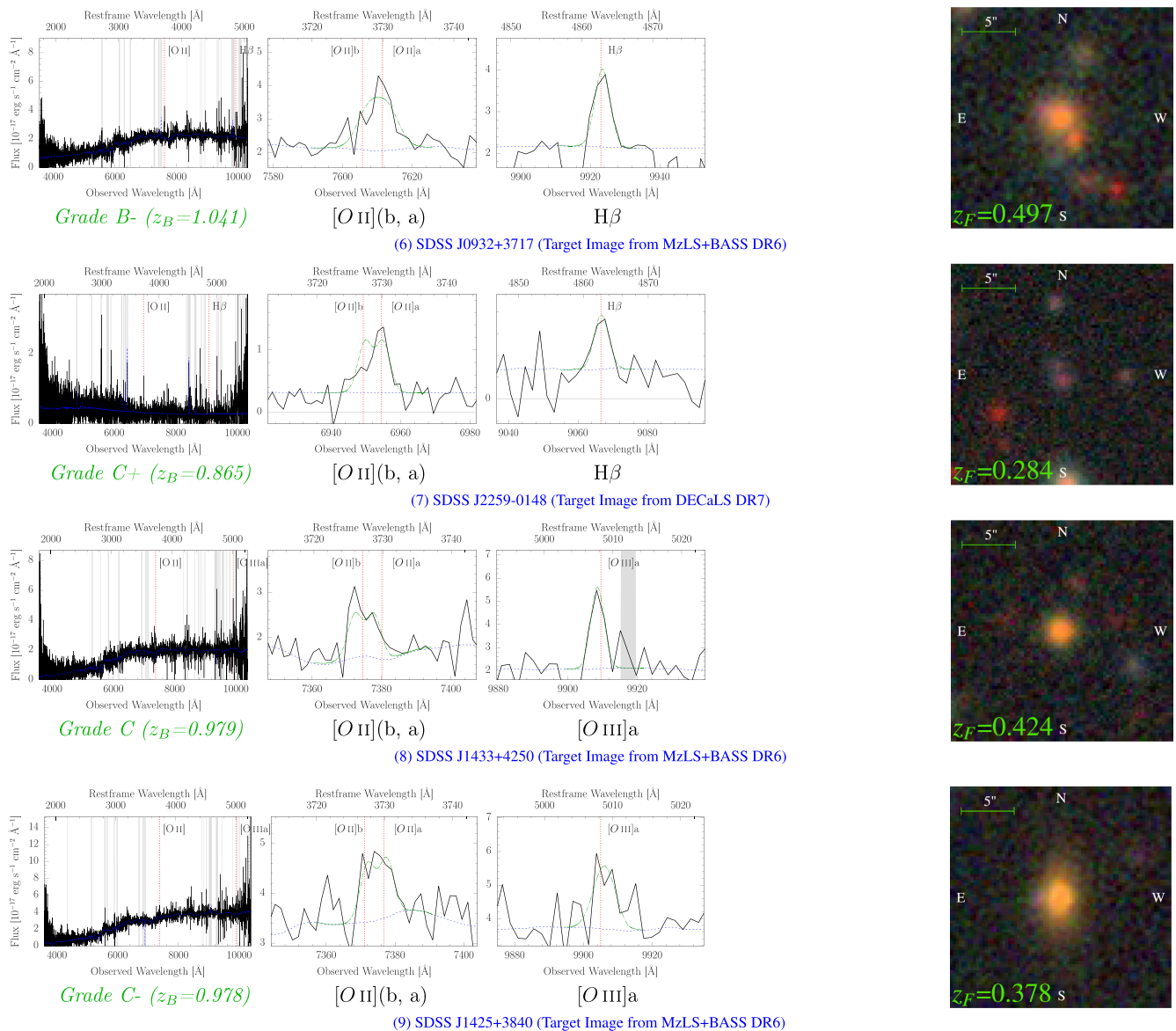


Figure 2. Continued. Examples of multi-line lens candidates, sorted by grade and selected in favour of candidates that might demonstrate a potential feature of lensing within a low-resolution image. Left: Plot of the target spectra and the position of the candidate background emission lines with an $\text{SN} \geq 4$. The grade and redshift are displayed below the plot in green. Centre: Plot of the flux, target model, and the appropriate Gaussian plus continuum model for each candidate emission line with an $\text{SN} \geq 4$. Within these plots, we represent the spectra with a black line, the foreground model with a dashed blue line, the fitted Gaussian model with a green dash-dotted line, and the positions of the candidate background emission lines with an $\text{SN} \geq 4$ with a red dotted vertical line. Masked regions of the flux are shaded with grey regions, which were not used in the generation of the background emission-line detections. Candidate lens SDSS J2259-0148 is an emission line-galaxy, which confirmation of a large number of emission-line lenses can be used to constrain the mass profiles of star-forming galaxies. This figure is continued.

Zheng et al. 1997; Vanden Berk et al. 2001; Osterbrock & Cohen 1982; Schaerer, Contini & Kunth 1999; Osterbrock & Fulbright 1996; Dhanda et al. 2007; Osterbrock, Shaw & Veilleux 1990; Persson 1988), which are recorded within the NIST Atomic Spectra Database (Kramida et al. 2019),¹ with the list of emission lines organized online here.² Candidate emission lines that exist within

$\approx \pm 4$ Angstroms of a target emission line are highly suspected if either the relative occurrence of detections or passing detections (see Section 3.7) is relatively high nearby, the width of a potentially affected $[\text{O II}]$ (b, a) imply a single emission line, the target emission line is known to be a source of contamination, or the region demonstrates other suspicious features identified from the first inspection.

(xi) Globally assess the trending quality and patterns observed within the signal revealed by the Gaussian fit information to alert the inspector to detections that contain either promising or questionable features.

¹NIST Atomic Spectra Database: <https://www.nist.gov/pml/atomic-spectra-database>.

²Table of target emission lines selected by Drew Chojnowski: <http://astronomy.nmsu.edu/drewski/tableofemissionlines.html>.

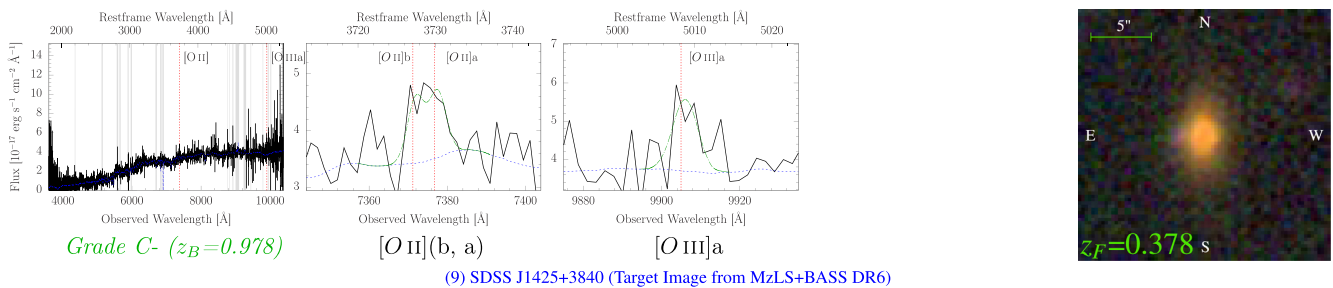


Figure 2. *Continued.* Examples of multi-line lens candidates, sorted by grade and selected in favour of candidates that might demonstrate a potential feature of lensing within a low-resolution image. Left: Plot of the target spectra and the position of the candidate background emission lines with an SN ≥ 4 . The grade and redshift are displayed below the plot in green. Centre: Plot of the flux, target model, and the appropriate Gaussian plus continuum model for each candidate emission line with an SN ≥ 4 . Within these plots, we represent the spectra with a black line, the foreground model with a dashed blue line, the fitted Gaussian model with a green dash-dotted line, and the positions of the candidate background emission lines with an SN ≥ 4 with a red dotted vertical line. Masked regions of the flux are shaded with grey regions, which were not used in the generation of the background emission-line detections.

(xii) Use the Gaussian information to observe if the shape of the [O II](b, a) doublet does not reasonably fit the [O II](b, a) Gaussian doublet. Candidate [O II](b, a) doublets that have a large reduced χ^2 are suspected as false-positives since the signal may lack the shape of an [O II](b, a) doublet.

(xiii) Use the Gaussian information to observe if the [O II](b, a) doublet fits an [O II](b, a) doublet Gaussian worse than a single Gaussian.

(xiv) Use the Gaussian information to flag if the full width at half-maximum (FWHM) of the [O II](b, a) doublet is less than the separation between the emission lines. Candidate [O II](b, a) doublets whose FWHM are less than the separation between the [O II](b, a) emission lines are rejected as false positives if no other assurances are present.

(xv) Examine the candidate emission line overlayed with the Gaussian fit model (see 3.3). This enabled the inspector to compare the candidate [O II](b, a) doublet with how the candidate would be approximately shaped by the redshift-dependent separation between the emission lines if the evaluated sigma of the model is typical of emission-line candidates.

(xvi) Highlight emission lines other than the [O II](b, a) doublet that demonstrate patterns expected of star-forming galaxies, such as detections with an [O III]a to [O III]b signature ratio of 3:1 in amplitude.

(xvii) Re-examine suspected regions and trends learned during the first iteration of inspection (see Section 3.7).

3.6 Inspection of lensing in low-resolution images

Detections that pass spectroscopic inspection are next examined for interfering objects and misidentified targets within the low-resolution images. The available images used are from the Legacy survey of SDSS-I/II and the Dark Energy Camera Legacy Survey (DECaLS), the Beijing-Arizona Sky Survey (BASS; Zou et al. 2017), and the Mayall z-band Legacy Survey (MzLS) survey within the Dark Energy Spectroscopic Instrument survey (DESI; DESI Collaboration et al. 2016; Dey et al. 2019). These images are obtained from the DESI sky server.³ We reject detections that demonstrate clear misidentifications within the low-resolution images. A total of 1263 single-line and 288 multi-line detections passed spectroscopic and imaging inspection to qualify as strong lensing candidates.

³DESI sky server: <http://legacysurvey.org/viewer>.

Though SILO candidates have not been confirmed by foreground subtraction from high-resolution images, we considered if indications of rings, multiple images, arcs, background galaxies within arc-seconds of the target, and possible overlapping colours of two galaxies may increase the assurances for a fair fraction of SILO detections. Inspiration for this additional method originates from the BELLS GALLERY survey, which published that 4 of 17 (24 per cent) of their confirmed lenses demonstrated lensing evidence within images of the target obtained from the Legacy survey of SDSS-I/II. However, the lensing evidence we expect to observe within SDSS images of SILO lens candidates cannot be directly equated to the BELLS GALLERY survey results since this survey used a sufficiently different spectroscopic selection method.

We can approximate the expected fraction of potential lensing features we can observe within SILO candidates to the fraction of lensing features observed in BELLS candidates since both surveys search the BOSS galaxies using the same detection method. We found $\frac{1}{5}$ of the BELLS candidates demonstrated indications of lensing, of which $\frac{2}{3}$ of these indications are observed in grade-A lenses, with one indication observed in a false-positive candidate. A search within low-resolution images of SILO candidates yielded a similar fraction of potential features of lensing (see Table 3).

The greatest difficulty of assessing the assurances from lensing evidence within low-resolution images is that un-lensed background galaxies, satellite galaxies, clumps of star formation within targets, and flaws in the images may be the cause of the observed feature. Thus only the more well-shaped lensing evidence is considered to carry some assurance within our inspection process. However, we are able to define a level of rarity for each type and quality of lensing evidence by comparing the ratio of ‘how often’ the indication occurs within SILO candidates to ‘how often’ the same indication occurs within 10,000 randomly selected galaxies from the BOSS and eBOSS surveys (see Table 3 and Table B2). Any relative increase in the occurrence of the indication observed by this method is most likely explained by the higher occurrence of either lensed or un-lensed background galaxies within SILO candidates.

These results enabled us to develop a total grading scheme that adds the rarity of the type and quality of lensing evidence upon the assurances indicated within the spectra by assessing ‘how unlikely’ the signal of a false spectroscopic detection matches patterns expected of emissions from a star-forming galaxy while

demonstrating a type and quality of lensing evidence within low-resolution images of the target. Thus, we derived a total grade based upon the grade assigned in spectroscopic inspection and biased by the rarity of the type and quality of a lensing evidence within each SILO candidate.

3.7 Iterative inspection method

Differences in the applied instrument, reduction, target selection method, and many other factors can impact the types of contamination observed within the spectra. Some of the more subtle issues and hidden trends can be realized after inspecting a large sample of detections. We added multiple iterations of the inspection process to help the inspector assess the impact of trends of assuring signals, known contaminants, and regions demonstrating suspicious features or relations to potential issues. Several examples of contaminants learned in the first inspection are: quasars misidentified as a galaxy and at a higher redshift than catalogued, the O I emission line misidentified as an [O II](b, a) doublet, and subtle differences between the sky emission and sky model can lead to significant residuals if the sky emission is strong. We also recorded the occurrence of passed detections per wavelength in both the rest frame and observed frame from the first inspection, which can help highlight regions of unexpected or underestimated contamination for the next cycle of inspection. This information enables the inspector to improve the grade of assurance assigned to the candidate during the final inspection process.

4 RESULTS

4.1 Count of strong-lensing candidates

We detected a total of 1551 (1263 single-line and 288 multi-line) candidates of various grades of assurance, with grade counts per search method, listed in Table 2). Of these candidates, 216 are from eBOSS targets, of which 146 are ELG targets. We assigned 838 (628 single-line and 210 multi-line) candidates a spectroscopic grade of A- or higher, and 919 with a total grade of A- or higher. If the grade-A lens probability function in SILO is similar to BELLS, then we can expect to confirm as many as ≈ 400 lenses within these candidates with a spectroscopic grade of A- or higher. Four candidate lenses contain a second background source at a higher redshift than the first background source, of which most are not highly assured, but are worth investigating as possible jackpot lenses (Bolton et al. 2008a), as they are extremely rare objects with 2 distinct Einstein Radii. At least 74 lens candidates have been previously discovered from other surveys, including 1 from the CAmbridge Sloan Survey Of Wide ARcs in the skY survey (CASSOWARY; Belokurov et al. 2009),⁴ 36 from the BELLS survey, 2 from the Strong Lensing Legacy Survey (SL2S; Gavazzi et al. 2012), 1 from Gavazzi et al. (2014), 26 from the SuGOHI (Sonnenfeld et al. 2018),⁵ 3 from Lenses in KiDS (LinKS; Petrillo et al. 2017, 2019),⁶ 3 from Jacobs et al. (2019), 1 from Huang et al. (2020b). Of these previously discovered candidates, 32 are reported as grade-A lenses from the Master Lens Database (Moustakas 2012). These previously discovered candidates are not cut from the VAC (see Section 5) to enable a complete

spectroscopic scan of the lensing probability function, and to be available for comparison to other surveys.

We obtained a 20 per cent increase in the number of detections over the expectation of lenses approximated in Section 2, which may be attributed to improvements in the final DR16 version (v5_13_0) of the eBOSS spectroscopic pipeline, and considerable improvements in our search method, as detailed in Section 3.

We provide examples of candidate emission lines with high SN along with low-resolution images of the target for multi-line lens candidates in Fig. 2 and single-line lens candidates in Fig. 3. These examples are sorted by grade, limited to three spectra plots per detection (for display ergonomics), with a selection in favour of targets that demonstrate lensing evidence within the low-resolution images. The grade and comment for each example are listed in Table B3 for multi-line detections and Table B4 for single-line detections, which are located in Appendix B. We note that these comments may describe features not displayed in the examples which impact the assigned grade.

Right: A low-resolution image of the candidate lens, which might display an indication that the system may be strongly lensed. The foreground redshift is presented in green on the image. Inspection comments for these candidates are listed in Table B3.

Right: A low-resolution image of the candidate lens, which might display an indication that the system may be strongly lensed. The foreground redshift is presented in green on the image. Inspection comments for these candidates are listed in Table B4.

4.2 Indications of lensing in the low-resolution images of the candidates

We observed 477 indications of lensing within low-resolution images of $\frac{1}{3}$ of the lens candidates. Examples of each type and quality of lensing evidence observed in SILO candidates are presented in Fig. 4, in which these images are obtained from the DESI survey. Table 3 lists the counts of each type of indicated lensing feature. At least $\frac{1}{3}$ of the identified lensing features include visible warping of the source image.

4.3 Comparisons of SILO to the BELLS survey

The search for lenses in these latest reductions yielded 16.4X the lens candidates detected over the BELLS survey with quality of signal approximate to the candidates from the BELLS survey. Since the BELLS survey searched the first $\frac{1}{13}$ of the BOSS survey, the fractional increase of our candidates reveals a $\frac{1}{4}$ increase in the detection rate of SILO. We also recovered 36 of the 45 BELLS candidates. The difference is primarily caused by two effects, due to which five grade-A lenses were not recovered. The first factor is that the BELLS detections were based on an earlier version of the pipeline from DR10, and pipeline improvements were made to optimize the foreground signal and redshift determination, which in some cases is less optimal for lens detection. The second factor is that some candidates were rejected for being located within newly detected regions of sky and target emission-line contamination that SILO resolved due to its larger sample of detections (see Section 3.4). Because SILO was limited to BOSS and eBOSS spectra, based on the new reductions included in the SDSS-IV DR16, there would not be any SLACS lenses in the SILO VAC since SDSS-III has not been re-processed since DR8.

We inspected the targets of the BELLS candidate blindly to validate if our spectroscopic grades of A- or higher are similar to the quality of signal observed within the BELLS candidates.

⁴CASSOWARY: <https://web1.ast.cam.ac.uk/ioa/research/cassowary/>.

⁵SuGOHI data base: <http://www-utap.phys.s.u-tokyo.ac.jp/~oguri/sugohi/>.

⁶LinKS Website: <https://www.astro.rug.nl/lensesinkids/>.

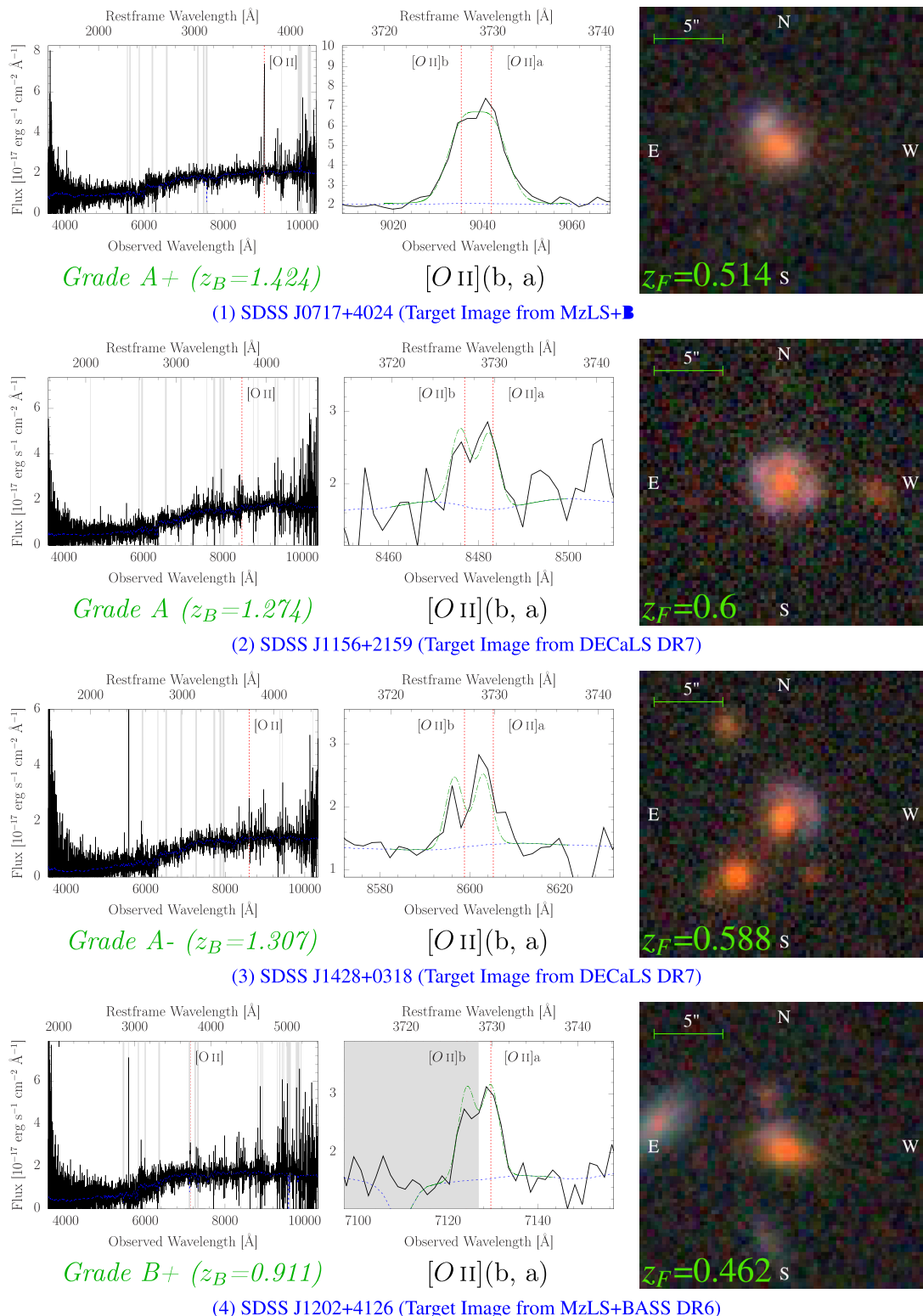


Figure 3. Examples of single-line lens candidates, sorted by grade and selected in favour of candidates that might demonstrate a potential feature of lensing within a low-resolution image, but not required. Left: Plot of the target spectra and the position of the candidate background emission lines with an SN ≥ 6 . The grade and redshift are displayed below the plot in green. Centre: Plot of the flux, target model, and the [O II](b, a) doublet Gaussian plus continuum model. Within these plots, we represent the spectra with a black line, the foreground model with a dashed blue line, the fitted Gaussian model with a green dash-dotted line, and the positions of the candidate background emission lines with an SN ≥ 4 with a red dotted vertical line. Masked regions of the flux are shaded with grey regions, which were not used in the generation of the background emission-line detections. This figure is continued.

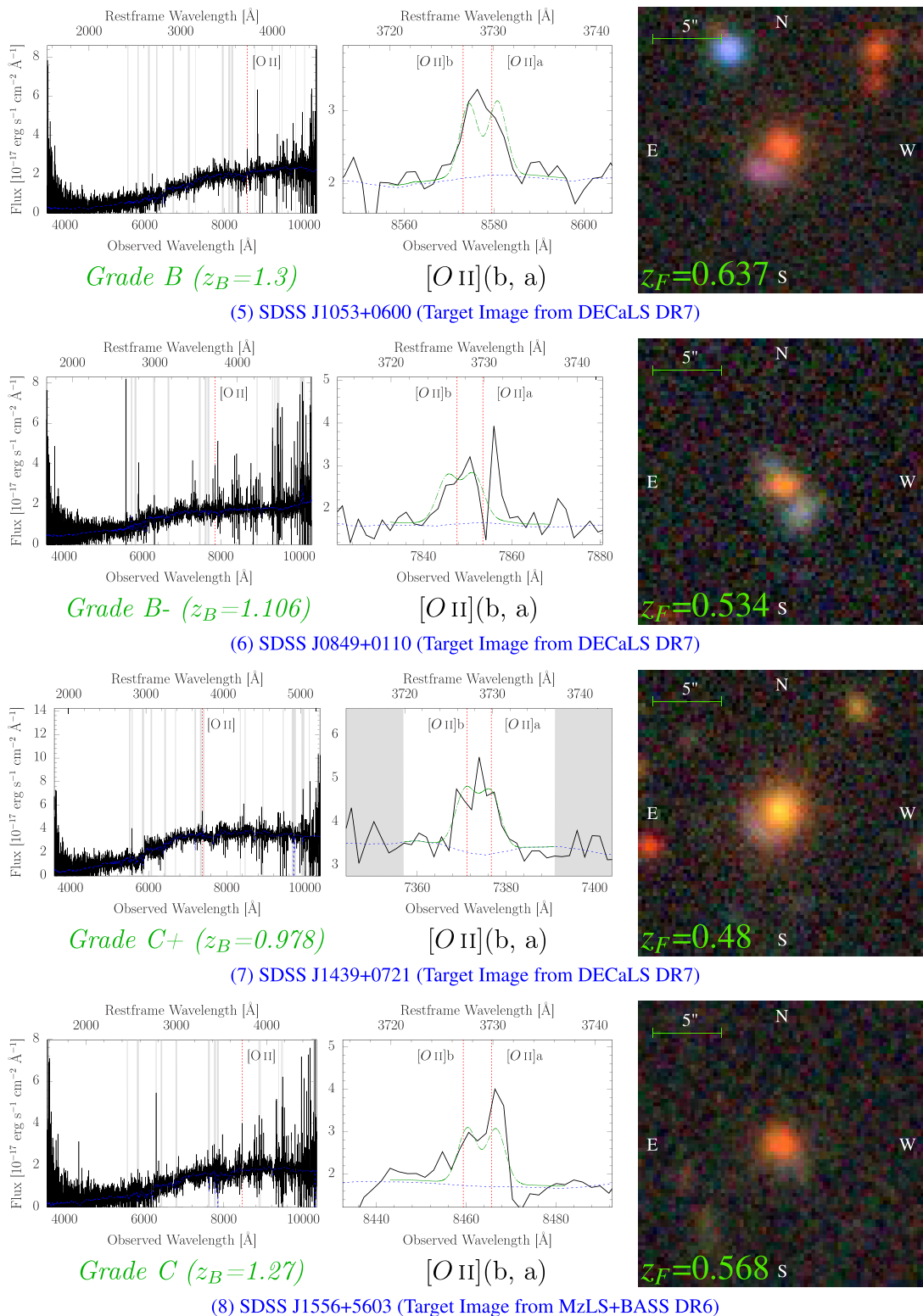


Figure 3. Continued. Examples of single-line lens candidates, sorted by grade and selected in favour of candidates that might demonstrate a potential feature of lensing within a low-resolution image, but not required. Left: Plot of the target spectra and the position of the candidate background emission lines with an $SN \geq 6$. The grade and redshift are displayed below the plot in green. Centre: Plot of the flux, target model, and the $[O\text{ II}](\text{b}, \text{a})$ doublet Gaussian plus continuum model. Within these plots, we represent the spectra with a black line, the foreground model with a dashed blue line, the fitted Gaussian model with a green dash-dot line, and the positions of the candidate background emission lines with an $SN \geq 4$ with a red dotted vertical line. Masked regions of the flux are shaded with grey regions, which were not used in the generation of the background emission-line detections. This figure is continued.

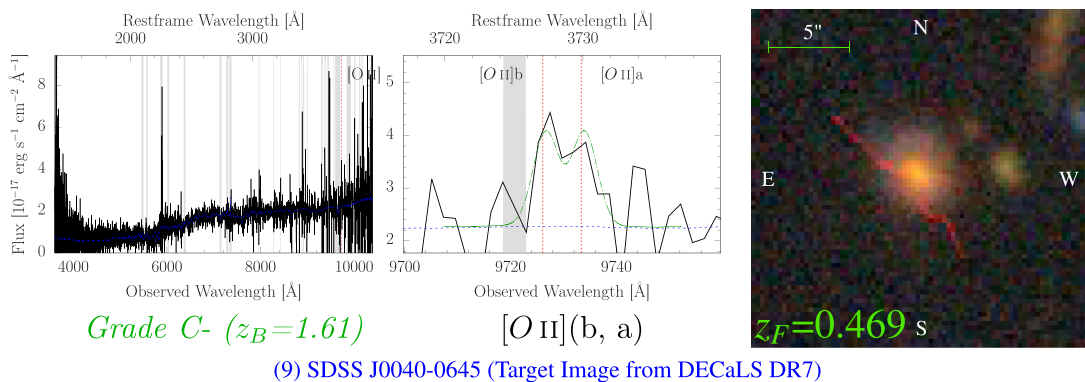


Figure 3. *Continued.* Examples of single-line lens candidates, sorted by grade and selected in favour of candidates that might demonstrate a potential feature of lensing within a low-resolution image, but not required. Left: Plot of the target spectra and the position of the candidate background emission lines with an SN ≥ 6 . The grade and redshift are displayed below the plot in green. Centre: Plot of the flux, target model, and the [O II](b, a) doublet Gaussian plus continuum model. Within these plots, we represent the spectra with a black line, the foreground model with a dashed blue line, the fitted Gaussian model with a green dash-dotted line, and the positions of the candidate background emission lines with an SN ≥ 4 with a red dotted vertical line. Masked regions of the flux are shaded with grey regions, which were not used in the generation of the background emission-line detections.

This test revealed that 76 per cent of the BELLS candidates within SILO are assigned a grade of A– or higher, 19 per cent are assigned a grade between B+ and B–, and 5 per cent are assigned a grade between C+ and C–. These results demonstrate that some ambiguity exists between the grade assigned by SILO to approximately represent the quality of signal observed within the BELLS candidates. This ambiguity may be caused by the differences in the reductions examined, the additional observations and inspection methods applied in SILO, or variances in the inspection criteria.

Fig. 5 demonstrates that the fractional redshift distribution of both the target and candidate background between SILO candidates and the BELLS candidates are similar. There is also an indication that the rejection rate of false-positives in the SILO project has improved over BELLS since the number density of candidates with lensing evidence within low-resolution images is 12 per cent higher for SILO when compared to BELLS.

5 PRESENTING THE STRONG LENS CANDIDATES IN A VAC

We included these lens candidates in a VAC in the Sixteenth Data Release (DR16) of SDSS, to enable future studies. This VAC also enables the public to examine the lens candidates that best suite their interest and to do follow-up observation.

The SILO VAC is located on the Science Archive Server⁷ (SAS) of SDSS and is divided into three types of files:

(i) The VAC contains a summary fits file (`silo_eboss_detections-1.0.1.fits`) that presents the detection, grade information, spectra, and comments derived from the manual inspection process. The extensions of the fits file are separated into survey information and emission lines searched in the primary extension, as shown in Table B5, detection information and data vectors of the spectra and model of the target, as shown in Table B6, and candidate emission-line data with Gaussian fit information for each candidate emission line with SN > 3 , as shown in Table B7. The columns of

this fits file are described and documented in the data model located on the SDSS server.⁸

(ii) The VAC contains plots of the candidate emission lines with a detection threshold of SN > 4 located in an `images` folder, organized by plate, with paths of the form `images/PLATE/flux-PLATE-MJD-FIBERID-HITID.png`. We include comments based on our manual inspection in the caption at the bottom of these plots, with details of the quality of the signal observed, including possible emission lines with SN < 4 that are below the threshold of the automated detection code and are only noticed during manual inspection.

(iii) The VAC contains low-resolution images of the target galaxy obtained from the Legacy survey of SDSS-I/II and the DESI surveys. We created 5 and 20 arcsec image cut-outs for each target for each survey the image was obtained from. We generated SDSS-I/II Legacy image cut-outs for all of our candidates. Since the footprints of the DESI imaging surveys partially overlap the locations of BOSS and eBOSS targets, we successfully generated DECaLS (DR7) image cut-outs for 1113 candidates and MzLS+BASS DR6 image cut-outs for 532 candidates. Note that some of the candidates have images from multiple imaging surveys. These files are located in the `images` folder, organized by plate, with filename prefixes corresponding to `sdss_image`, `decals_image`, or `mzls_bass_image`, with either a -5.png or -20.png file extension for the 5 and 20 arcsec cut-outs, respectively.

6 CONCLUSION AND DISCUSSION

6.1 Summary

We extended the Spectroscopic Identification of Lensing Objects (SILO) project to search the ≈ 2 million galaxy spectra contained within the BOSS and eBOSS data of SDSS DR16. Our spectroscopic detection algorithm is based upon the method applied in the BELLS survey and includes manual inspection grades, best-fitting Gaussian distributions to background emission lines, low-resolution images of

⁷SILO VAC on SAS: https://data.sdss.org/sas/dr16/eboss/spectro/lensing/silo/v5_13_0/v5_13_0/1.0.1/.

⁸SILO VAC Data model: https://data.sdss.org/datamodel/files/EBOSS_SPECTRO_LENSING/silo/RUN2D/RUN1D/SILO_VER/silo_eboss_detections.html.

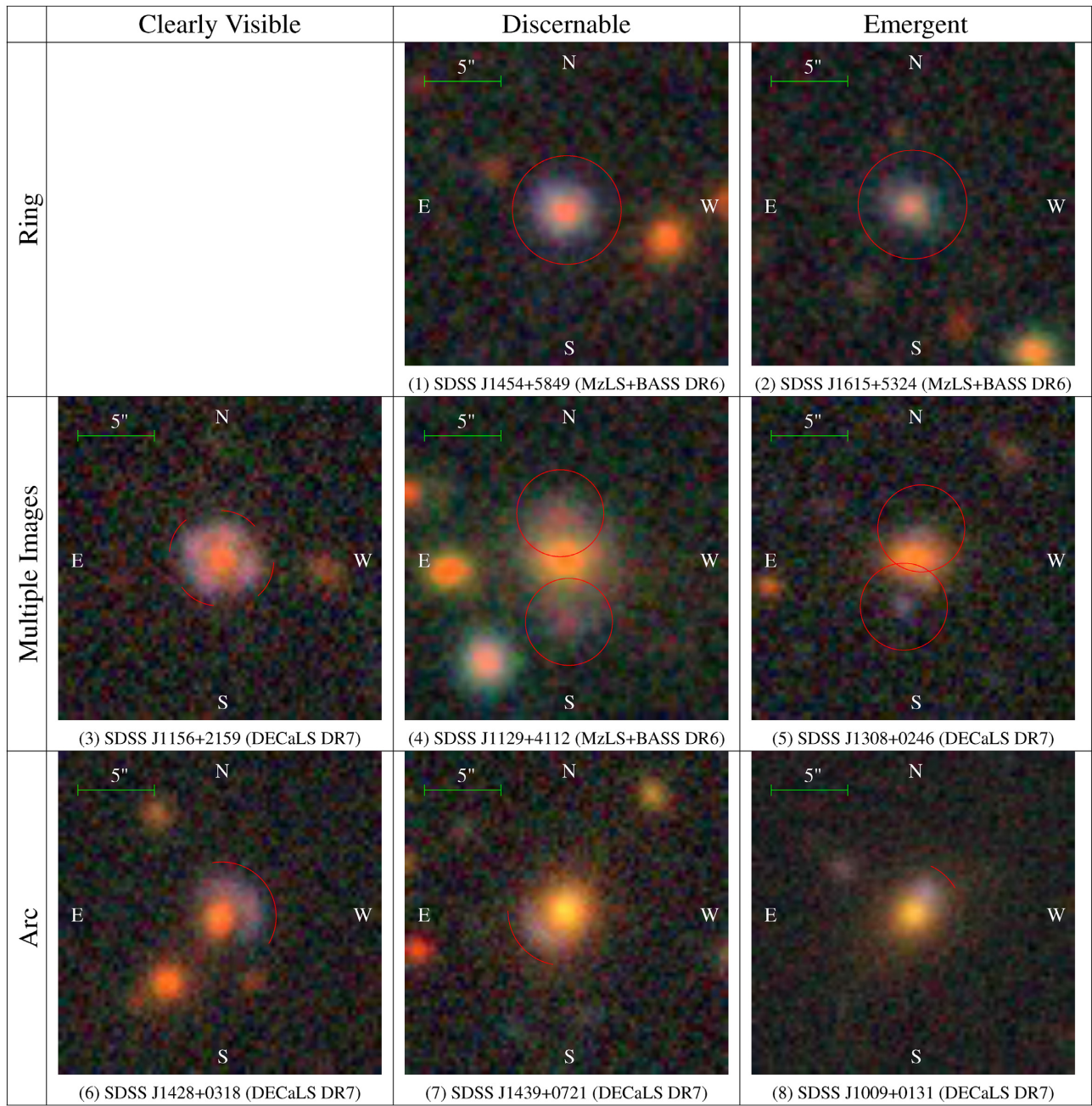


Figure 4. Examples of the type and quality of potential features of lensing within low-resolution images of strong lens candidates. Columns left to right display one clearly visible, one discernable, and one emergent indication of a specific type of potential feature of lensing, sorted from top to bottom for ring, multiple images, arc, possible source radially nearby to the lens, and mixed colours of the possible overlap of the source and lens. Red circles are placed to indicate possible rings or lensed images while red arcs are placed near possible source arcs. Strong features indicating probable strong lensing are presented in this first set of images. This figure is continued.

the target, and other spectroscopic observables to better assess each candidate and reject more false-positives. Of the 1551 (288 multi-line and 1263 single-line) strong lensing candidates within SILO, 838 are approximate in quality to the 45 candidates found within the BELLS survey. The selection rate of SILO candidates within the BOSS survey is $\approx \frac{1}{4}$ higher than the selection rate in the BELLS survey, which may be attributed to the search for lens candidates in the improved reductions of the BOSS data in DR16, the additional information used in the manual inspection process, and changes in the inspection criteria.

Though these strong lens candidates have not been observed by high-resolution imaging, 477 of the candidates demonstrate lensing evidence found within the low-resolution images from the Legacy survey of SDSS-I/II and the DESI Legacy survey. The fraction of potential features of lensing within SILO candidates is 12 per cent higher than observed within the BELLS candidates.

We produced a value-added catalog (VAC) for the mini Data Release 16 of SDSS-IV, as described in Section 5, which includes plots of the candidate emission lines, low-resolution images of the target, and a summary fits file containing data for the lens candidates.

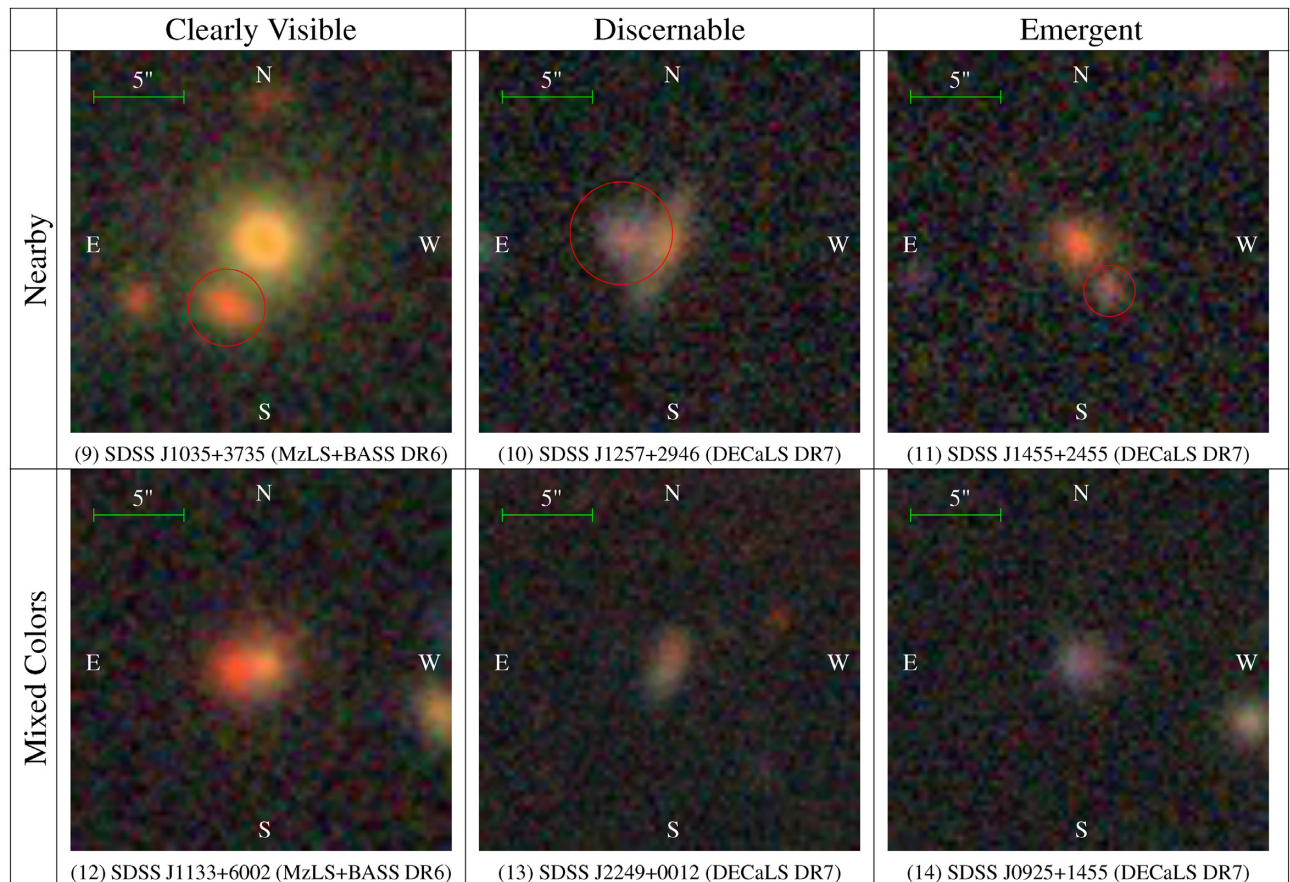


Figure 4. *Continued.* Examples of the type and quality of potential features of lensing within low-resolution images of strong lens candidates. Columns left to right display one clearly visible, one discernable, and one emergent indication of a specific type of potential feature of lensing, sorted from top to bottom for ring, multiple images, arc, possible source radially nearby the lens, and mixed colours of the possible overlap of the source and lens. Red circles are placed to indicate possible rings or lensed images while red arcs are placed near possible source arcs. Weaker features indicating possible strong lensing are presented in this figure.

The 74 lens candidates previously cited by previous surveys are referenced within the VAC.

6.2 Discussion of how confirmed SILO lenses can contribute to galaxy formation studies and future lens searches

Assuming a BELLS similar detection rate of grade-A lenses, we anticipate that ≈ 400 grade-A lenses can be confirmed from the lens candidates with a spectroscopic grade of A- or higher. Thus follow-up high-resolution imaging of SILO candidates may confirm over twice the number of known lenses that are spectroscopically detected within the SDSS surveys. Such a large sample of lenses can complement the results of previous surveys, enable new research objectives to be obtained, and provide resources to other search programmes. We provide several examples of the applications that SILO lenses may contribute to the lensing community in the following paragraphs.

The LRG lenses found within the Legacy survey of SDSS-I/II contained target redshifts up to ~ 0.55 , while SILO candidates contain target redshifts up to 1.1 and candidate source redshifts up to 1.713. Thus, follow-up imaging of the LRG lens candidates from SILO can extend the observations from lenses within the Legacy survey by twice the redshift, enabling farther and tighter constraints on time-

dependent and time-independent properties and formation models of LRGs (see Section 1).

Even a moderate sample of ELG lenses can significantly improve the current understanding of the mass profiles within ELGs, since this area of research is less constrained. For example, the SWELLS survey spectroscopically detected 20 high-inclination disk galaxy lenses within the Legacy survey of SDSS-I/II Treu et al. (2011) which was used to statistically verify their findings (Brewer et al. 2012) from a few disc lenses that a Chabrier IMF is favoured over a Salpeter IMF for disk galaxies (Dutton et al. 2011; Barnabè et al. 2012). The SWELLS survey also used this sample to probe the IMF of the disc and bulge of disc galaxies (Brewer et al. 2014). Confirming a large sample of lenses from the 146 ELG lens candidates in SILO may provide sufficient resources to better separate and examine the mass components of the bulge, disk, and halo of spiral galaxies (Keeton & Kochanek 1998).

We observe that lens searches within either images or spectra often provide resources that may be beneficial to the other search method, while candidates from one search method are rarely found by the other. The first observation that supports our reasoning is that few of the lens candidates are being detected by both imaging and spectroscopic search methods due to the physical limits of the search methods. Two recent examples of image-based search methods that

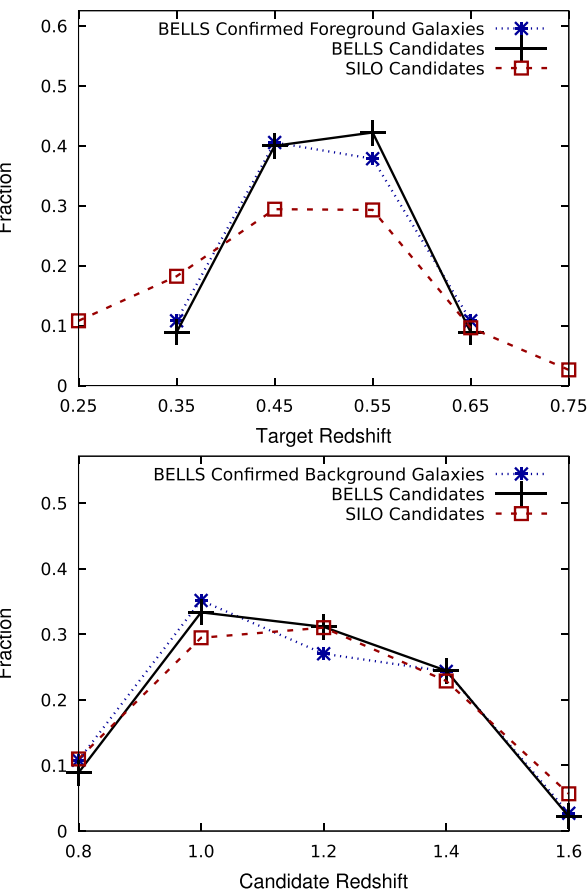


Figure 5. Comparison of the fractional distribution of the target (top) and detection redshifts (bottom) between the SILO candidates, the candidates of the BELLS survey, and the confirmed lenses of the BELLS survey.

affirm a fraction of our SILO detections in SDSS DR16 are: as follows:

(i) Huang et al. (2020a) report on a search for ‘new’ strong gravitational lenses within the DESI Legacy Imaging Surveys, which has detected 10 SILO candidates (DESI- 036.0992 + 02.4337, DESI-217. 0936 + 03.3000, DESI- 219.9040 + 07.3502, DESI- 341.8329 + 18.0226, DESI- 132.2802 + 22.0446, DESI-205.8655 + 21.7388, DESI-219.1501 + 21.1453, DESI-233.2341 + 50.1953, DESI-160.7046 + 62.6611, DESI-010.0606- 06.7620).

(ii) The Highly Optimised Lensing Investigations of Supernovae, Microlensing Objects, and Kinematics of Ellipticals and Spirals (HOLISMOKES; Cañameras et al. 2020) which has affirmed 7 SILO candidates (PS1J0737 + 1914, PS1J0907 + 4233, PS1J1233 + 1407, PS1J0917 + 3109, PS1J1134 + 1712, PS1J2233 + 3012, PS1J1105 + 5503).

Some image search methods subtract the lens light in images to reveal lensed features behind the relatively dominant light of the lens (Joseph et al. 2014). While this method can work on high-resolution images, subtraction of the lens light can remove source features within lower resolution or lower SN images (Brault & Gavazzi 2015). Other methods have tried to separate or examine colour differences between the lens and source (Gavazzi et al. 2014; Maturi, Mizera & Seidel 2014). The most recently applied image searches methods typically use machine learning to search for potential source features (Kubo & Dell’Antonio 2008; Marshall

et al. 2009; Ostrovski et al. 2017; Petrillo et al. 2017, 2019; Pearson, Pennock & Robinson 2018; Avestruz et al. 2019; Jacobs et al. 2019; Huang et al. 2020b). However, the only sources effectively detected by these methods are located beyond the relatively dominating and interfering light of the lens. Thus the detection of the source images by these methods typically requires the Einstein radius of the lens to be fairly larger than 1 arcsec. In contrast, spectroscopically detected lenses from the SLACS, BELLS, BELLS GALLERY, and SWELLS surveys rarely demonstrate an Einstein radius significantly larger than 1 arcsec, since the 1–1.5 arcsec radius of the fibre limits the solid angle the source can be effectively detected within. Thus, the combined lenses from both image and spectroscopic detection methods can yield a large sample of lenses with a distribution of Einstein radii across most of a galactic profile while neither method can effectively recover the candidates obtained from applying the other method. Confirmation of a large sample of lenses found by SILO within the MaNGA, BOSS, and eBOSS surveys can populate the relatively under-represented distributions of Einstein radii across the LRG galactic profile, which populations cannot be obtained from either the lenses in the Legacy survey of SDSS or the lenses from the image search programs described here.

Our second observation is that both search methods utilize image and spectroscopic information, ranging from understanding how to develop a search method to confirmation and examination of the source and lens. Also, spectra and image combined searches are developing as large spectroscopic surveys (such as BOSS and eBOSS within SDSS-III/IV) and large low/higher resolution imaging surveys (such as DESI or HSC-SSP; Aihara et al. 2018) are observing many of the same targets. The SuGOHI survey has developed a spectra and image combined search method that subtracts the lens light from the images and spectra to detect background emission lines within the BOSS spectra and lensing evidence within HSC-SSP images. The SuGOHI survey has searched at least $\frac{1}{20}$ of the BOSS galaxy spectra and found at least 26 of the lens candidates contained within the SILO VAC. SILO has also included image information into its spectroscopic inspection process by examining low-resolution images of the spectroscopically selected candidates (see Section 3.6), which enabled us to compare if certain types and quality of lensing evidence occur more often in spectroscopically selected candidates (see Table 3) than in a random sample of BOSS and eBOSS galaxies (see Table B2). The image information enabled us to improve the assurances for $\frac{1}{3}$ of our candidates and may provide information to lens searches within low-resolution images about large-scale trends of lensing evidence supported by spectroscopic detection. Confirmation of SILO lens candidates can test if these trends have merit in any future image or spectroscopic searches within DESI and SDSS.

ACKNOWLEDGEMENTS

Funding for the Sloan Digital Sky Survey IV has been provided by the Alfred P. Sloan Foundation, the U.S. Department of Energy Office of Science, and the Participating Institutions.

SDSS-IV acknowledges support and resources from the Center for High Performance Computing at the University of Utah. The SDSS website is www.sdss.org.

SDSS-IV is managed by the Astrophysical Research Consortium for the Participating Institutions of the SDSS Collaboration including the Brazilian Participation Group, the Carnegie Institution for Science, Carnegie Mellon University, Center for Astrophysics/Harvard & Smithsonian, the Chilean Participation Group, the French Participation Group, Instituto de Astrofísica de Canarias,

The Johns Hopkins University, Kavli Institute for the Physics and Mathematics of the Universe (IPMU) / University of Tokyo, the Korean Participation Group, Lawrence Berkeley National Laboratory, Leibniz Institut für Astrophysik Potsdam (AIP), Max-Planck-Institut für Astronomie (MPIA Heidelberg), Max-Planck-Institut für Astrophysik (MPA Garching), Max-Planck-Institut für Extraterrestrische Physik (MPE), National Astronomical Observatories of China, New Mexico State University, New York University, University of Notre Dame, Observatório Nacional / MCTI, The Ohio State University, Pennsylvania State University, Shanghai Astronomical Observatory, United Kingdom Participation Group, Universidad Nacional Autónoma de México, University of Arizona, University of Colorado Boulder, University of Oxford, University of Portsmouth, University of Utah, University of Virginia, University of Washington, University of Wisconsin, Vanderbilt University, and Yale University.

DATA AVAILABILITY

The data described in this paper are available to the public at https://data.sdss.org/sas/dr16/eboss/spectro/lensing/silo/v5_1_3.0/v5_13.0/1.0.1 and are described at https://www.sdss.org/dr16/da_ta_access/value-added-catalogs/?vac_id = eboss-strong-gravitational-lens-detection-catalog.

REFERENCES

- Abolfathi B. et al., 2018, *ApJS*, 235, 42
 Ahn C. P. et al., 2014, *ApJS*, 211, 17
 Ahumada R. et al., 2020, *ApJS*, 249, 3
 Aihara H. et al., 2018, *PASJ*, 70, S8
 Alam S. et al., 2015, *ApJS*, 219, 12
 Albareti F. D. et al., 2017, *ApJS*, 233, 25
 Alloin D., Bica E., Bonatto C., Prugniel P., 1992, *A&A*, 266, 117
 Arneson R. A., Brownstein J. R., Bolton A. S., 2012, *ApJ*, 753, 4
 Auger M. W., Treu T., Bolton A. S., Gavazzi R., Koopmans L. V. E., Marshall P. J., Moustakas L. A., Burles S., 2010, *ApJ*, 724, 511
 Avastruz C., Li N., Zhu H., Lightman M., Collett T. E., Luo W., 2019, *ApJ*, 877, 58
 Barnabè M., Czoske O., Koopmans L. V. E., Treu T., Bolton A. S., Gavazzi R., 2009, *MNRAS*, 399, 21
 Barnabè M. et al., 2012, *MNRAS*, 423, 1073
 Belokurov V., Evans N. W., Hewett P. C., Moiseev A., McMahon R. G., Sanchez S. F., King L. J., 2009, *MNRAS*, 392, 104
 Benson A. J., 2020, *MNRAS*, 493, 1268
 Blanton M. R. et al., 2017, *AJ*, 154, 28
 Bolton A. S., Burles S., Koopmans L. V. E., Treu T., Moustakas L. A., 2006, *ApJ*, 638, 703
 Bolton A. S., Burles S., Koopmans L. V. E., Treu T., Gavazzi R., Moustakas L. A., Wayth R., Schlegel D. J., 2008a, *ApJ*, 682, 964
 Bolton A. S., Treu T., Koopmans L. V. E., Gavazzi R., Moustakas L. A., Burles S., Schlegel D. J., Wayth R., 2008b, *ApJ*, 684, 248
 Bolton A. S. et al., 2012, *AJ*, 144, 144
 Brammer G. B. et al., 2012, *ApJ*, 758, L17
 Brault F., Gavazzi R., 2015, *A&A*, 577, A85
 Brewer B. J. et al., 2012, *MNRAS*, 422, 3574
 Brewer B. J., Marshall P. J., Auger M. W., Treu T., Dutton A. A., Barnabè M., 2014, *MNRAS*, 437, 1950
 Brownstein J. R. et al., 2012, *ApJ*, 744, 41
 Bundy K. et al., 2015, *ApJ*, 798, 7
 Cabanac R. A., Valls-Gabaud D., Lidman C., 2008, *MNRAS*, 386, 2065
 Cañameras R. et al., 2020, *A&A*, 644, A163
 Cao S., Biesiada M., Yao M., Zhu Z.-H., 2016, *MNRAS*, 461, 2192
 Collett T. E., Auger M. W., Belokurov V., Marshall P. J., Hall A. C., 2012, *MNRAS*, 424, 2864
 Cornachione M. A. et al., 2018, *ApJ*, 853, 148
 Dawson K. S. et al., 2013, *AJ*, 145, 10
 Dawson K. S. et al., 2016, *AJ*, 151, 44
 DESI Collaboration et al., 2016, preprint (<arXiv:1611.00036>)
 Despali G., Vegetti S., White S. D. M., Giocoli C., van den Bosch F. C., 2018, *MNRAS*, 475, 5424
 Dey A. et al., 2019, *AJ*, 157, 168
 Dhabra N., Baldwin J. A., Bentz M. C., Osmer P. S., 2007, *ApJ*, 658, 804
 Dutton A. A. et al., 2011, *MNRAS*, 417, 1621
 Ferland G. J., Osterbrock D. E., 1987, *ApJ*, 318, 145
 Fukugita M., Futamase T., Kasai M., 1990, *MNRAS*, 246, 24P
 Gavazzi R., Treu T., Koopmans L., Bolton A., Moustakas L., Burles S., Marshall a., 2008, *ApJ*, 677, 1046
 Gavazzi R., Treu T., Marshall P. J., Brault F., Ruff A., 2012, *ApJ*, 761, 170
 Gavazzi R., Marshall P. J., Treu T., Sonnenfeld A., 2014, *ApJ*, 785, 144
 Gunn J. E. et al., 2006, *AJ*, 131, 2332
 Hewett P. C., Warren S. J., Willis J. P., Bland -Hawthorn J., Lewis G. F., 2000, in van Breugel W., Bland-Hawthorn J., eds, ASP Conf. Ser. Vol. 195, Imaging the Universe in Three Dimensions. Astron. Soc. Pac., San Francisco, p. 94
 Hezaveh Y. D. et al., 2016, *ApJ*, 823, 37
 Huang X. et al., 2020a, *AAS*, 53, 125.04
 Huang X. et al., 2020b, *ApJ*, 894, 78
 Izotov Y. I., Chaffee F. H., Schaerer D., 2001, *A&A*, 378, L45
 Izotov Y. I., Papaderos P., Guseva N. G., Fricke K. J., Thuan T. X., 2004, *A&A*, 421, 539
 Jacobs C. et al., 2019, *ApJS*, 243, 17
 Gee I., Komatsu E., Suyu S. H., 2015, *J. Cosmol. Astropart. Phys.*, 2015, 033
 Joseph R. et al., 2014, *A&A*, 566, A63
 Keeton C. R., Kochanek C. S., 1998, *ApJ*, 495, 157
 Keeton C. R., Kochanek C. S., Falco E. E., 1998, *ApJ*, 509, 561
 Kochanek C. S., 1995, *ApJ*, 445, 559
 Komossa S. et al., 2008, *ApJ*, 678, L13
 Koopmans L. V. E., 2005, *MNRAS*, 363, 1136
 Koopmans L. V. E., Treu T., Bolton A. S., Burles S., Moustakas L. A., 2006, *ApJ*, 649, 599
 Koopmans L. V. E. et al., 2009, *ApJ*, 703, L51
 Kramida A., Ralchenko Y., Reader J., and NIST ASD Team, 2019, NIST Atomic Spectra Database (ver. 5.7.1). National Institute of Standards and Technology, Gaithersburg, MD [Online]. Available: <https://physics.nist.gov/asd> [Tuesday, 20-Sep-2011 13:19:04 EDT]
 Kubo J. M., Dell'Antonio I. P., 2008, *MNRAS*, 385, 918
 Lagattuta D. J., Vegetti S., Fassnacht C. D., Auger M. W., Koopmans L. V. E., McKean J. P., 2012, *MNRAS*, 424, 2800
 Leighly K. M., Moore J. R., 2004, *ApJ*, 611, 107
 Li R., Shu Y., Wang J., 2018, *MNRAS*, 480, 431
 Linder E. V., 2016, *Phys. Rev. D*, 94, 083510
 Lupton R., Gunn J. E., Ivezić Ž., Knapp G. R., Kent S., 2001, in Harnden F. R. J., Primini F. A., Payne H. E., eds, ASP Conf. Ser. Vol. 238, Astronomical Data Analysis Software and Systems X. Astron. Soc. Pac., San Francisco, p. 269
 Marshall P. J. et al., 2007, *ApJ*, 671, 1196
 Marshall P. J., Hogg D. W., Moustakas L. A., Fassnacht C. D., Bradač M., Schrabback T., Blandford R. D., 2009, *ApJ*, 694, 924
 Maturi M., Mizera S., Seidel G., 2014, *A&A*, 567, A111
 Moustakas L., 2012, The Master Lens Database and The Orphan Lenses Project. AAS, HST Proposal
 Mukherjee S., Koopmans L. V. E., Metcalf R. B., Tortora C., Schaller M., Schaye J., Vernardos G., Bellagamba F., 2019, preprint (<arXiv:1901.01095>)
 Nightingale J. W., Massey R. J., Harvey D. R., Cooper A. P., Etherington A., Tam S.-I., Hayes R. G., 2019, *MNRAS*, 489, 2049
 Oldham L. et al., 2017, *MNRAS*, 465, 3185
 Osterbrock D. E., Cohen R. D., 1982, *ApJ*, 261, 64
 Osterbrock D. E., Fulbright J. P., 1996, *PASP*, 108, 183
 Osterbrock D. E., Pogge R. W., 1985, *ApJ*, 297, 166
 Osterbrock D. E., Shaw R. A., Veilleux S., 1990, *ApJ*, 352, 561
 Ostrovski F. et al., 2017, *MNRAS*, 465, 4325

- Pearson J., Pennock C., Robinson T., 2018, Emergent Scientist, 2, 1
- Persson S. E., 1988, *ApJ*, 330, 751
- Petillo C. E. et al., 2017, *MNRAS*, 472, 1129
- Petillo C. E. et al., 2019, *MNRAS*, 484, 3879
- Puchnarewicz E. M., Mason K. O., Siemiginowska A., 1998, *MNRAS*, 293, L52
- Rose M., Tadhunter C. N., Holt J., Ramos Almeida C., Littlefair S. P., 2011, *MNRAS*, 414, 3360
- Schaerer D., Contini T., Kunth D., 1999, *A&A*, 341, 399
- Shu Y. et al., 2015, *ApJ*, 803, 71
- Shu Y. et al., 2016, *ApJ*, 824, 86
- Smee S. A. et al., 2013, *AJ*, 146, 32
- Sonnenfeld A., Treu T., Gavazzi R., Suyu S. H., Marshall P. J., Auger M. W., Nipoti C., 2013, *ApJ*, 777, 98
- Sonnenfeld A. et al., 2018, *PASJ*, 70, S29
- Sonnenfeld A., Jaelani A. T., Chan J., More A., Suyu S. H., Wong K. C., Oguri M., Lee C.-H., 2019, *A&A*, 630, A71
- Spinello C., Koopmans L. V. E., Trager S. C., Czoske O., Treu T., 2011, *MNRAS*, 417, 3000
- Talbot M. S. et al., 2018, *MNRAS*, 477, 195
- Thuan T. X., Izotov Y. I., 2005, *ApJS*, 161, 240
- Tran H. D., Cohen M. H., Villar-Martín M., 2000, *AJ*, 120, 562
- Treu T., Dutton A. A., Auger M. W., Marshall P. J., Bolton A. S., Brewer B. J., Koo D. C., Koopmans L. V. E., 2011, *MNRAS*, 417, 1601
- Vanden Berk D. E. et al., 2001, *AJ*, 122, 549
- Vegetti S., Koopmans L. V. E., Bolton A., Treu T., Gavazzi R., 2010, *MNRAS*, 408, 1969
- Vegetti S., Lagattuta D. J., McKean J. P., Auger M. W., Fassnacht C. D., Koopmans L. V. E., 2012, *Nature*, 481, 341
- Vegetti S., Koopmans L. V. E., Auger M. W., Treu T., Bolton A. S., 2014, *MNRAS*, 442, 2017
- Wang T.-G., Zhou H.-Y., Wang L.-F., Lu H.-L., Xu D., 2011, *ApJ*, 740, 85
- Warren S. J., Hewett P. C., Lewis G. F., Møller P., Iovino A., Shaver P. A., 1996, *MNRAS*, 278, 139
- Willis J. P., Hewett P. C., Warren S. J., 2005, *MNRAS*, 363, 1369
- Willis J. P., Hewett P. C., Warren S. J., Dye S., Maddox N., 2006, *MNRAS*, 369, 1521
- York D. G. et al., 2000, *AJ*, 120, 1579
- Zheng W., Kriss G. A., Telfer R. C., Grimes J. P., Davidsen A. F., 1997, *ApJ*, 475, 469
- Zou H. et al., 2017, *PASP*, 129, 064101

APPENDIX A: OPTIMIZATION OF GAUSSIAN FITS

SILO optimizes Gaussian fitting to the residual flux by implementing a gridded parameter search to find the grid with the lowest χ^2 , set the limits of the next grid search within the boundaries of the chosen grid, and repeat this process until the parameters of the fit do not vary significantly between iterations. While this

method quickly converges on a fit, the initial range of possible values for each parameter must encompass the parameters of the global minimum and not be so extreme that the χ^2 map created by the optimizer is poorly resolved. Thus, we must provide the optimizer with a reasonable range of spectra to set the initial search range.

We set the range of the initial grid search based upon the information contained within the search algorithm applied by the BELLS survey and the features demonstrated by the signal. We used a test sigma (σ_{test}) from the BELLS survey of 2.4 pixels as a ‘ruler’ used in selecting samples of spectra and evaluating the range of most parameters used in the grid search. Since the pixels of BOSS spectra are $\approx 1 \text{ \AA}$ in size, σ_{test} also approximates the typical sigma observed in single emission lines of confirmed background galaxies within the BELLS survey.

We select a sample of the wavelength vector, residual flux, and inverse variance within $4 \sigma_{\text{test}}$ of the location of a candidate emission line determined by the detection program. We select twice this range of data for any candidate [O II](b, a) doublet since the width of an [O II](b, a) is approximately twice a single emission line.

Our choice of limits on each parameter is calibrated based on trial fits followed by visual inspection of the quality and robustness of the Gaussian fit. We strictly set the initial search range of wavelengths within one σ_{test} of the expected location of the candidate emission line to prevent the optimizer from fitting any noisy features nearby when the SN of the candidate emission line is low. We set the initial search range of amplitudes within three times the difference in the residual flux, centred on the maximum value of the residual flux, and evaluated either within one σ_{test} of the location of a single emission line or one σ_{test} plus the spacing between the [O II](b, a) emission lines. The maximum sigma the optimizer can search is set to twice the sigma approximated from the shape of the emission line within the residual flux.

To set the initial range in searchable heights, we first find the local median in the residual flux located either between 5 and 15 σ_{test} of the location of a single emission line, or twice these ranges for a candidate [O II](b, a) doublet. We then set the initial range in searchable heights around twice the median of the median. Performance tests of the search range on the fit parameters revealed that we also must constrain the height to be positive as to prevent a negative bias in the fitted height caused by differences between the Gaussian model and semi-Gaussian signal.

APPENDIX B: TABLES

See Tables B1–B7.

Table B1. Spectroscopic grading criteria used in the inspection process. Column 1 lists the grades a candidate can be assigned. Column 2 lists the criteria for each grade. Grades can be appended with a sign of + or – to indicate if the assurances within the spectra are more or less than the stated criteria.

Grade (1)	Criteria (2)
Grade A	The signal is judged as likely by at least two $\text{SN} \geq 4$ candidate background emission lines demonstrate one of the following: (i) Clear patterns of a star-forming galaxy, which any potential contamination is unlikely to interfere with the quality of the signal significantly. (ii) Patterns demonstrate minor differences from the expected pattern of a star-forming galaxy and whose high $\text{SN} \approx \geq 12$ dominates any potential contamination. (iii) Patterns demonstrate minor differences from the expected pattern of a star-forming galaxy with additional $\text{SN} \leq 4$ emission line(s) to assure that the pattern is unlikely to be generated from any potential contamination.
Grade B	The signal is judged as probable by at least two $\text{SN} \geq 4$ candidate background emission lines that demonstrate one of the following: (i) Patterns demonstrate no less than some difference from the patterns expected of a star-forming galaxy. (ii) Patterns demonstrate little difference from the patterns expected of a star-forming galaxy that are overlapped by suspected regions of influential contamination. (iii) Signal demonstrates a milder combination of the quality and contamination issues of 1 and 2. (iv) Signal would have been assigned a Grade C but is reinforced by the presence of other potential emission lines.
Grade C	The signal is judged as possible by at least two $\text{SN} \geq 4$ candidate background emission lines that demonstrate one of the following: (i) Patterns demonstrate a significant difference from the patterns expected of a star-forming galaxy. (ii) Patterns demonstrate little difference from the patterns expected of a star-forming galaxy and are located within suspected regions of dominant contamination. (iii) Signal demonstrates a milder combination of the quality and contamination issues of 1 and 2. (iv) The two $\text{SN} \geq 4$ emission lines are evaluated as unlikely to indicate a background galaxy but are reinforced by the presence of other potential emission lines.

Table B2. Counts of the types and quality of potential features of lensing observed within 10,000 low-resolution images of BOSS and eBOSS targets obtained from the DESI Legacy survey, which control sample is used to assess the rarity of each potential feature of lensing. Column 1 lists the type of potential lensing feature, while columns 2 through 4 list how discernable is the feature.

Indication Type (1)	Clearly Visible (2)	Discernible (3)	Emergent (4)
Ring	0	3	15
Multiple images or arcs	0	3	5
Arc	1	25	77
Possible source radially nearby the lens	10	51	341
Possible overlapping colours of two galaxies	17	252	312
Total	28	334	750

Table B3. This table lists the System Name in Column 1, the Spectroscopic and Total Grades in Columns 2 and 3, and the Manual Inspection Comment in Column 4, for multi-line examples in Fig. 2.

System name (1)	Spectroscopic (2)	Total (3)	Manual inspection comment (4)
SDSS J0213C-0347	A+	A+	Well-formed [O II](b, a). Shape of [O II](b, a) best matches a double Gaussian. SN greater than 12 for [O II](b, a). Well-formed [O III](b, a) 1/3 pattern. Multiple emission-line evidence. Emergent H δ . Emergent H γ . Well-formed H β . Well-formed [O III]b. Well-formed [O III]a. SN greater than 12 for [O III]a. Potential sky contamination near [O II](b, a). Sky emissions located near left side of candidate emission line is approximate or less than 20×10^{-17} erg s $^{-1}$ cm $^{-2}$ Ang $^{-1}$. Nearby sky emission(s) are either relatively insignificant or misaligned to previously stated candidate emission, and thus less likely to cause a false emission line generated from undersubtraction. Occurrence of detections observed in rest frame near left side of candidate emission line is more common than the local median around [O II](b, a). Potential sky contamination near H δ . Sky emissions located near doublet is approximate or less than 20×10^{-17} erg s $^{-1}$ cm $^{-2}$ Ang $^{-1}$. Nearby sky emission(s) are either relatively insignificant or misaligned to previously stated candidate emission, and thus less likely to cause a false emission line generated from undersubtraction. Potential sky contamination near H γ . Sky emissions located near left side of candidate emission line is approximate or less than 20×10^{-17} erg s $^{-1}$ cm $^{-2}$ Ang $^{-1}$. Nearby sky emission(s) are either relatively insignificant or misaligned to previously stated candidate emission, and thus less likely to cause a false emission line generated from undersubtraction. Visual inspection of image reveal supportive indications of an arc (discernable in DECaLS image and SDSS image), which implies a total grade of A+.
SDSS J1152+2753	A	A+	Discernable [O II](b, a). Shape of [O II](b, a) best matches a double Gaussian. Multiple emission-line evidence. Emergent [O III]b. Discernable [O III]a. Potential sky contamination near [O II](b, a). Sky emissions located near right side of candidate emission line is approximately between 20×10^{-17} and 30×10^{-17} erg s $^{-1}$ cm $^{-2}$ Ang $^{-1}$. Nearby sky emission(s) are either relatively insignificant or misaligned to previously stated candidate eion, and thus less likely to cause a false emission line generated from undersubtraction. Occurrence of detections observed in rest frame near right side of candidate emission line is significantly more common than the local median around [O III]a. Visual inspection of image reveal supportive indications of an arc (discernable in DECaLS image and SDSS image), which implies a total grade of A+.
SDSS J0731+3635	A-	A	Signal width matches [O II](b, a). Shape of [O II](b, a) best matches a mix between double and single Gaussian. Multiple emission-line evidence. Emergent H β . Well-formed [O III]a. Potential sky contamination near [O II](b, a). Sky emissions located near centre of candidate emission line is approximate or greater than 30×10^{-17} erg s $^{-1}$ cm $^{-2}$ Ang $^{-1}$. Sky emissions located near left side of candidate emission line is approximate or less than 20×10^{-17} erg s $^{-1}$ cm $^{-2}$ Ang $^{-1}$. Visual inspection of image reveal supportive indications of possible mix ed colours of background object with foreground target (emergent in MzLS + BASS image), which implies a total grade of A.
SDSS J0009-0501	B+	A+	Discernable [O II](b, a). Shape of [O II](b, a) best matches a mix between double and single Gaussian. Multiple emission-line evidence. Discernable [O III]a. Potential sky contamination near [O II](b, a). Sky emissions located near right side of candidate emission line is approximate or greater than 30×10^{-17} erg s $^{-1}$ cm $^{-2}$ Ang $^{-1}$. Sky emissions located near left side of candidate emission line is approximate or greater than 30×10^{-17} erg s $^{-1}$ cm $^{-2}$ Ang $^{-1}$. Candidate emission line [O II](b, a) might be mistaken as foreground [Fe vi]. Occurrence of detections observed in rest frame near left side of candidate emission line is significantly more common than the local median around [O II](b, a). Occurrence of detections observed in rest frame near right side of candidate emission line is more common than the local median around [O II](b, a). Visual inspection of image reveal supportive indications of an arc (emergent in DECaLS image and SDSS image), which implies a total grade of A+.
SDSS J0955+6231	B	A+	Emergent [O II](b, a). Shape of [O II](b, a) best matches a mix between double and single Gaussian. Multiple emission-line evidence. Emergent H β . Discernable [O III]a. Potential sky contamination near [O II](b, a). Sky emissions located near centre of candidate emission line is approximate or less than 20×10^{-17} erg s $^{-1}$ cm $^{-2}$ Ang $^{-1}$. Nearby sky emission(s) are either relatively insignificant or misaligned to previously stated candidate emission, and thus less likely to cause a false emission line generated from undersubtraction. Potential sky contamination near H β . Candidate emission line [O III]a might be mistaken as foreground [Ar I]. Visual inspection of image reveal supportive indications of an arc (emergent in SDSS image), which implies a total grade of A+.

Table B3 – *continued*

System name (1)	Spectroscopic (2)	Total (3)	Manual inspection comment (4)
SDSS J0932+3717	BC–	B +	Discernable [O II](b, a). Shape of [O II](b, a) best matches a single Gaussian. Multiple emission-line evidence. Discernable H β . Potential sky contamination near [O II](b, a). Sky emissions located near right side of candidate emission line is approximate or less than 20×10^{-17} erg s $^{-1}$ cm $^{-2}$ Ang $^{-1}$. Sky emissions located near left side of candidate emission line is approximate or less than 20×10^{-17} erg s $^{-1}$ cm $^{-2}$ Ang $^{-1}$. Suspicious calibration variance or sky model variance observed. Sky contamination H β . Visual inspection of image reveal supportive indications of possible mix ed colours of background object with foreground target (emergent in MzLS+BASS image and SDSS image), which implies a total grade of B + .
SDSS J2259C–0148	C +	B–	Discernable [O II](b, a). Shape of [O II](b, a) best matches a mix between double and single Gaussian. Multiple emission-line evidence. Emergent H β . Emergent [O III]b. Discernable [O III]a. Potential sky contamination near [O II](b, a). Sky emissions located near left side of candidate emission line is approximately between 20×10^{-17} and 30×10^{-17} erg s $^{-1}$ cm $^{-2}$ Ang $^{-1}$. Nearby sky emission(s) are either relatively insignificant or misaligned to previously stated candidate emission, and thus less likely to cause a false emission line generated from undersubtraction. Occurrence of detections observed in rest frame near centre of candidate emission line is significantly more common than the local median around [O II](b, a). Potential sky contamination near [O III]b. Potential sky contamination near [O III]a. Visual inspection of image reveal supportive indications of possible mix ed colors of background object with foreground target (emergent in DECaLS image), which implies a total grade of B–.
SDSS J1433+4250	C	C	Emergent [O II](b, a). Shape of [O II](b, a) best matches a double Gaussian. Multiple emission-line evidence. Well-formed [O III]a. Potential sky contamination near [O II](b, a). Sky emissions located near left side of candidate emission line is approximately between 20×10^{-17} and 30×10^{-17} erg s $^{-1}$ cm $^{-2}$ Ang $^{-1}$. Evidence observed that undersubtraction influenced signal. Potential sky contamination near [O III]a. Nearby sky emission(s) are either relatively insignificant or miss aligned to previously stated candidate emission, and thus less likely to cause a false emission line generated from undersubtraction. Occurrence of detections observed in rest frame near left side of candidate emission line is significantly more common than the local median around [O III]a.
SDSS J1425+3840	C–	BC–	Shape of [O II](b, a) best matches a mix between double and single Gaussian. Multiple emission-line evidence. Emergent [O III]a. Potential sky contamination near [O II](b, a). Sky emissions located near left side of candidate emission line is approximate or greater than 30×10^{-17} erg s $^{-1}$ cm $^{-2}$ Ang $^{-1}$. Nearby sky emission(s) are either relatively insignificant or misaligned to previously stated candidate emission, and thus less likely to cause a false emission line generated from undersubtraction. Visual inspection of image reveal supportive indications of nearby object (emergent in MzLS + BASS image and SDSS image), which implies a total grade of B–.

Table B4. This table lists the System Name in Column 1, the Spectroscopic and Total Grades in Columns 2 and 3, and the Manual Inspection Comment in Column 4, for single-line examples in Fig. 3.

System name (1)	Spectroscopic (2)	Total (3)	Manual inspection comment (4)
SDSS J0717+4024	A+	A+	Well-formed [O II](b, a). Shape of [O II](b, a) best matches a double Gaussian. SN greater than 12 for [O II](b, a). Potential sky contamination near [O II](b, a). Sky emissions located near centre of candidate emission line is approximate or less than 20×10^{-17} erg s $^{-1}$ cm $^{-2}$ Ang $^{-1}$. Sky emissions located near right side of candidate emission line is approximate or less than 20×10^{-17} erg s $^{-1}$ cm $^{-2}$ Ang $^{-1}$. Nearby sky emission(s) are either relatively insignificant or misaligned to previously stated candidate emission, and thus less likely to cause a false emission line generated from undersubtraction. [O II](b, a) doublet feature is indicated in individual exposures. Visual inspection of image reveal supportive indications of several arcs (discernable in MzLS+BASS image and SDSS image), which implies a total grade of A + .
SDSS J1156+2159	A	A+	Emergent [O II](b, a). Shape of [O II](b, a) best matches a double Gaussian. Potential sky contamination near [O II](b, a). Sky emissions located near left side of candidate emission line is approximate or greater than 30×10^{-17} erg s $^{-1}$ cm $^{-2}$ Ang $^{-1}$. Nearby sky emission(s) are either relatively insignificant or misaligned to previously stated candidate emission, and thus less likely to cause a false emission line generated from undersubtraction. Visual inspection of image reveal supportive indications of a quad (well formed in DECaLS image and SDSS image), which implies a total grade of A + .

Table B4 – *continued*

System name (1)	Spectroscopic (2)	Total (3)	Manual inspection comment (4)
SDSS J1428+0318	A–	A+	Discernable [O II](b, a). Shape of [O II](b, a) best matches a double Gaussian. Potential sky contamination near [O II](b, a). Sky emissions located near left side of candidate emission line is approximate or less than 20×10^{-17} erg s $^{-1}$ cm $^{-2}$ Ang $^{-1}$. Nearby sky emission(s) are either relatively insignificant or misaligned to previously stated candidate emission, and thus less likely to cause a false emission line generated from undersubtraction. Visual inspection of image reveal supportive indications of an arc (well formed in DECaLS image and SDSS image), which implies a total grade of A + .
SDSS J1202+4126	B+	A–	Discernable [O II](b, a). Shape of [O II](b, a) best matches a double Gaussian. Occurrence of pre-inspection passed detections observed in rest frame near centre of candidate emission line is slightly more common than the local median around [O II](b, a). Visual inspection of image reveal supportive indications of possible mix ed colours of background object with foreground target (emergent in MzLS+BASS image), which implies a total grade of A–.
SDSS J1053+0600	B	A	Discernable [O II](b, a). Shape of [O II](b, a) best matches a mix between double and single Gaussian. Candidate emission line [O II](b, a) might be mistaken as foreground [Fe IV]. Doublet signal is wider than a typical single emission line. Visual inspection of image reveal supportive indications of an arc (discernable in DECaLS image and SDSS image), which implies a total grade of A.
SDSS J0849+0110	B–	A+	Discernable [O II](b, a). Potential sky contamination near [O II](b, a). Sky emissions located near right side of candidate emission line is approximate or greater than 30×10^{-17} erg s $^{-1}$ cm $^{-2}$ Ang $^{-1}$. Sky emissions located near left side of candidate emission line is approximately between 20×10^{-17} and 30×10^{-17} erg s $^{-1}$ cm $^{-2}$ Ang $^{-1}$. Visual inspection of image reveal supportive indications of several arcs (well formed in DECaLS image and SDSS image), which implies a total grade of A + .
SDSS J1439+0721	C+	A+	Discernable [O II](b, a). Shape of [O II](b, a) best matches a triple Gaussian. Potential sky contamination near [O II](b, a). Sky emissions located near centre of candidate emission line is approximate or greater than 30×10^{-17} erg s $^{-1}$ cm $^{-2}$ Ang $^{-1}$. Sky emissions located near left side of candidate emission line is approximate or less than 20×10^{-17} erg s $^{-1}$ cm $^{-2}$ Ang $^{-1}$. Visual inspection of image reveal supportive indications of an arc (discernable in DECaLS image and SDSS image), which implies a total grade of A + .
SDSS J1556+5603	C	B–	Discernable [O II](b, a). Shape of [O II](b, a) best matches a mix between double and single Gaussian. Potential sky contamination near [O II](b, a). Sky emissions located near right side of candidate emission line is approximately between 20×10^{-17} and 30×10^{-17} erg s $^{-1}$ cm $^{-2}$ Ang $^{-1}$. Sky emissions located near left side of candidate emission line is approximate or less than 20×10^{-17} erg s $^{-1}$ cm $^{-2}$ Ang $^{-1}$. Nearby sky emission(s) are either relatively insignificant or misaligned to previously stated candidate emission, and thus less likely to cause a false emission line generated from undersubtraction. Visual inspection of image reveal supportive indications of possible mix ed colours of background object with foreground target (emergent in MzLS + BASS image), which implies a total grade of B–.
SDSS J0040–0645	C–	B+	Discernable [O II](b, a). Shape of [O II](b, a) best matches a double Gaussian. Potential sky contamination near [O II](b, a). Sky emissions located near left side of candidate emission line is approximate or greater than 30×10^{-17} erg s $^{-1}$ cm $^{-2}$ Ang $^{-1}$. Sky emissions located near right side of candidate emission line is approximately between 20×10^{-17} and 30×10^{-17} erg s $^{-1}$ cm $^{-2}$ Ang $^{-1}$. Suspicious calibration variance or sky model variance observed. Occurrence of pre-inspection passed detections observed in rest frame near centre of candidate emission line is significantly more common than the local median around [O II](b, a). Visual inspection of image reveal supportive indications of a ring (emergent in DECaLS image and SDSS image), which implies a total grade of B + .

Table B5. This table lists the headers of the primary extension of the fits file within the SILO VAC. Column 1 lists the identifier of the data. Column 2 lists the value of the header. Column 3 lists the unit type. Column 4 lists the format type. Column 5 lists the description of each header or table column.

Name (1)	Value (2)	Unit (3)	Type (4)	Description (5)
PROJECT	SILO		String	Lens search project
AUTHORS	Michael Talbot		String	SILO project creators
INSP	Michael Talbot		String	Detection inspector
SCANNED	BOSS+eBOSS		String	SDSS surveys scanned by SILO
SILO_VER	1.0.1		String	Version of SILO project used
RUN1D	V5.13.0		String	BOSS/eBOSS 1D reduction version of spectra
RUN2D	V5.13.0		String	BOSS/eBOSS 2D reduction version of spectra
RELEASE	DR16		String	SDSS data release version
SAMPLING	LOG		String	Wavelength sampling of spectra
SPECTYPE	COADDED		String	Type of spectra searched
OIIB	3727.092	Å	Float	Rest-frame wavelength of OIIb
OIIA	3729.875	Å	Float	Rest-frame wavelength of OIIa
HID	4102.892	Å	Float	Rest-frame wavelength of HID
HIC	4341.684	Å	Float	Rest-frame wavelength of HIC
HIB	4862.683	Å	Float	Rest-frame wavelength of HIB
OIIIB	4960.295	Å	Float	Rest-frame wavelength of OIIIb
OIIIA	5008.239	Å	Float	Rest-frame wavelength of OIIIa
NIIB	6549.86	Å	Float	Rest-frame wavelength of NIIb
HIA	6564.614	Å	Float	Rest-frame wavelength of HIA
NIIA	6585.27	Å	Float	Rest-frame wavelength of NIIa
SIIB	6718.29	Å	Float	Rest-frame wavelength of SIIb
SIIA	6732.68	Å	Float	Rest-frame wavelength of SIIa

Table B6. This table lists the columns within the DETECTION extension of the fits file within the SILO VAC. Column 1 lists the identifier of the data. Column 2 lists the unit type. Column 3 lists the format type. Column 4 lists the description of each header or table column.

Name (1)	Unit (2)	Type (3)	Description (4)
CATALOG_ID		Integer	Detection identifier for this catalogue
EMLINE_SCAN_TYPE		String	Background emission line search mode: Single-line=OII(b, a) with SN >= 6, Multi-line=2 + emission lines with SN >= 4
DETECTION_Z		Float	Redshift of background candidate
N_EMLINES_SN_GE4		Integer	Number of emission lines detected with SN >= 4
QUADRATURE_SUM_SN_GE3		Float	Quadrature sum of emission lines with SN >= 3
SPECTRA_GRADE		String	Grade of spectra assurances of source candidate
TOTAL_GRADE		String	Grade of spectra and image assurances of candidate
COMMENT		String	Comment of assuring/non-assuring features
FIRST_DETECTION_FROM		String	Identity of earlier discoverer
FIRST_DETECTION_LG		String	Strong lens grade from Masterlens database
SDSS_TARGET_NAME		String	SDSS RA+Dec. name of target
PLATE		Integer	Plate number of BOSS/eBOSS observation of target
MJD		Integer	Modified Julian Day on observation of target
FIBER_INDEX		Integer	Fibre on plate used for observation
SDSS_SURVEY		String	SDSS survey the spectra was obtained from
BESTOBJID		String	SDSS unique database ID of (recommended) position-based photometric match based on RUN, RERUN, CAMCOL, FIELD, ID (same as SkyServer version)
SPECOBJID		String	Unique database ID based on PLATE, MJD, FIBERID, RUN2D (same as SkyServer version)
CLASS_NOQSO		String	SDSS non-quasar classification of target
OBJCLASS		String	SDSS classification of target
TARGET_GALAXY_TYPE		String	SDSS classification of type of target galaxy (i.e. ELG, LRG). Variable is named SOURCETYPE in eBOSS.
TARGETOBJID		String	SDSS unique database ID of targeting object based on RUN, RERUN, CAMCOL, FIELD, ID (same as SkyServer version)
Z_NOQSO		Float	SDSS best redshift when ignoring QSO fits, recommended for BOSS CMASS and LOWZ targets; calculated only for survey = 'boss' spectra, not for any SDSS spectrograph data
ZERR_NOQSO		Float	Error in Z_NOQSO redshift

Table B6 – *continued*

Name (1)	Unit (2)	Type (3)	Description (4)
ZWARNING_NOQSO		Integer	SDSS bitmask of spectroscopic warning values; 0 means everything is OK
RA	Degree	Float	Target right ascension
DEC	Degree	Float	Target declination
RA_HMS	hour:':'	String	Target right ascension in hour:min:sec
DEC_DMS	Degree:':'	String	Target declination in degree:min:sec
WAVE	Å	Float (Array)	Wavelength vector of spectra from BOSS/eBOSS
FLUX	$10^{-17} \text{ erg s}^{-1} \text{ cm}^{-2} \text{ Å}^{-1}$	Float (Array)	Coadded object flux from BOSS/eBOSS
IVAR		Float (Array)	Inverse variance of spectra from BOSS/eBOSS
AND_MASK		Integer (Array)	and._mask of coadded spectra from BOSS/eBOSS
OR_MASK		Integer (Array)	or._mask of coadded spectra from BOSS/eBOSS
SKY	$10^{-17} \text{ erg s}^{-1} \text{ cm}^{-2} \text{ Å}^{-1}$	Float (Array)	Coadded sky emissions from BOSS/eBOSS
WDISP	$10^{-17} \text{ erg s}^{-1} \text{ cm}^{-2} \text{ Å}^{-1}$	Float (Array)	Wavelength dispersion of spectra from BOSS/eBOSS
MODEL_SILO	$10^{-17} \text{ erg s}^{-1} \text{ cm}^{-2} \text{ Å}^{-1}$	Float (Array)	Foreground model generated by SILO
IVAR_RESCALED		Float (Array)	Rescaled inverse variance
RESIDUAL_FLUX	$10^{-17} \text{ erg s}^{-1} \text{ cm}^{-2} \text{ Å}^{-1}$	Float (Array)	Residual flux of FLUX-MODEL_SILO
SN_SPECTRA_SG		Float (Array)	Gaussian convolved S/N of spectra

Table B7. This table lists the columns within the EMISSION_LINE_ANALYSIS extension of the fits file within the SILO VAC. Column 1 lists the identifier of the data. Column 2 list the unit type. Column 3 list the format type. Column 4 lists the description of each header or table column.

Name (1)	Unit (2)	Type (3)	Description (4)
DETECTION_CATALOG_ID		Integer	Detection identifier for this catalogue
NAME		String	Name of emission line
INDEX_IN_SPECTRA		Integer	Index where emission line is located in spectra
EM_WAVE	Å	Flux	Wavelength of emission line computed from rest-frame wavelength $\times (1 + z)$
SN		Float	Gaussian convolved S/N of emission line
GAUSS_FIT_REPORTED		Boolean	Gauss fit reported if SN $>= 3$
GAUSS_WAVE	Å	Float (Array)	Wavelength(s) centre of Gaussian model with $-/+$ from 2.5, 97.5 quartiles from Monte Carlo simulation
GAUSS_BASE_HEIGHT	$10^{-17} \text{ erg s}^{-1} \text{ cm}^{-2} \text{ Å}^{-1}$	Float (Array)	Gaussian model base height with $-/+$ from 2.5, 97.5 quartiles from Monte Carlo simulation
GAUSS_AMPLITUDE	$10^{-17} \text{ erg s}^{-1} \text{ cm}^{-2} \text{ Å}^{-1}$	Float (Array)	Gaussian model amplitude with $-/+$ from 2.5, 97.5 quartiles from Monte Carlo simulation
GAUSS_SIGMA	Å	Float (Array)	Gaussian model sigma with $-/+$ from 2.5, 97.5 quartiles from Monte Carlo simulation
RCHI2_SAMPLE		Float	Reduced χ^2 of Gaussian fit to spectra sample
NDOF_SAMPLE		Integer	Degree of freedom of RCHI2_SAMPLE
RCHI2_3SIG		Float	Reduced χ^2 of Gaussian fit within 3 sigma of the model
NDOF_3SIG		Integer	Degree of freedom of RCHI2_3SIG
SAMPLE_SIZE		Integer	Size of spectra sample used in Gaussian Fit
MODEL_WAVE_BASE	Å	Float (Array)	Wavelength base of Gaussian model
GAUSS_MODEL	$10^{-17} \text{ erg s}^{-1} \text{ cm}^{-2} \text{ Å}^{-1}$	Float (Array)	Gaussian model of residual flux
FITTED_RESIDUAL_FLUX	$10^{-17} \text{ erg s}^{-1} \text{ cm}^{-2} \text{ Å}^{-1}$	Float (Array)	Residual flux segment used in Gaussian fit
FITTED_IVAR_RESCALED		Float (Array)	Rescaled inverse variance used in Gauss fit
AND_MASK		Integer (Array)	SDSS AND_MASK of sample of spectra
OR_MASK		Integer (Array)	SDSS OR_MASK of sample of spectra

This paper has been typeset from a TeX/LaTeX file prepared by the author.